WILEY-VCH

DOI: 10.1002/adfm.201707319
Article type: Full Paper

Copper (I) Selenocyanate (CuSeCN) as a Novel Hole-Transport Layer for Transistors, Organic Solar Cells and Light-Emitting Diodes

*Nilushi Wijeyasinghe, Leonidas Tsetseris, Anna Regoutz, Wai-Yu Sit, Zhuping Fei, Tian Du, Xuhua Wang, Martyn A. McLachlan, George Vourlias, Panos A. Patsalas, David J. Payne, Martin Heeney, and Thomas D. Anthopoulos**

N. Wijeyasinghe, W.-Y. Sit, Dr. X. Wang, Prof. T. D. Anthopoulos
Department of Physics and the Centre for Plastic Electronics
Imperial College London
London SW7 2AZ, UK

Prof. L. Tsetseris
Department of Physics
National Technical University of Athens
Athens GR-15780, Greece

Dr. A. Regoutz, Mr. T. Du, Dr. M. A. McLachlan, Dr. D. J. Payne
Department of Materials and the Centre for Plastic Electronics
Imperial College London
Royal School of Mines, London SW7 2AZ, UK

Dr. P. A. Patsalas, Dr. G. Vourlias
Department of Physics
Laboratory of Applied Physics
Aristotle University of Thessaloniki
Thessaloniki 54124, Greece

Dr. Z. Fei, Prof. M. Heeney
Department of Chemistry and The Centre for Plastic Electronics
Imperial College London, London SW7 2AZ, UK

Prof. T. D. Anthopoulos
King Abdullah University of Science and Technology (KAUST)
Division of Physical Sciences and Engineering and KAUST Solar Centre
Thuwal 23955-6900, Saudi Arabia
E-mail: thomas.anthopoulos@kaust.edu.sa

Keywords: Copper (I) selenocyanate; hole transport layers; organic solar cells; organic light-emitting diodes; transparent semiconductors

Abstract

We report the synthesis and characterization of copper (I) selenocyanate (CuSeCN) and its application as a solution-processable hole-transport layer (HTL) material in transistors, organic light-emitting diodes and solar cells. Density-functional theory calculations combined with X-ray photoelectron spectroscopy were used to elucidate the electronic band structure, density of states and microstructure of CuSeCN. Solution-processed layers are found to be nanocrystalline and optically transparent (>94%), due to the large bandgap of ≥3.1 eV, with a valence band maximum located at -5.1 eV. Hole-transport analysis performed using field effect measurements confirmed the *p*-type character of CuSeCN yielding a hole mobility of 0.002 $cm^2V^{-1}s^{-1}$. When CuSeCN was incorporated as the HTL material in organic light-emitting diodes and organic solar cells, the resulting devices exhibit comparable or improved performance to control devices based on commercially available poly(3,4-ethylenedioxythiophene) polystyrene sulfonate (PEDOT:PSS) as the HTLs. This is the first report on the semiconducting character of CuSeCN and highlights the tremendous potential for further developments in the area of metal pseudohalides.

1. Introduction

There is currently an immense demand for *p*-type semiconductors that can function as hole-transport layer (HTL) materials in emerging opto/electronic technologies.[1–3] This is primarily because significant improvements in device performance can be achieved when a suitable HTL is added between the anode and the active layer in various types of devices including organic photovoltaic (OPV) cells.[4,5] Remarkable improvements in device performance are also reported in organic light emitting diodes (OLEDs) employing either a hole-injection layer (HIL) such as molybdenum oxide (MoO_x) in addition to an HTL,[6,7] or a dual function HIL/HTL such as nickel oxide (NiO_x).[8] An ideal universal interlayer needs to be an inexpensive and

chemically stable material, which exhibits layer uniformity, high optical transparency, good solvent orthogonality with subsequently processed layers, appropriate energy level alignment with common active layer materials, and low-temperature processability over large-area substrates. Despite a number of promising developments in recent years, due to these stringent requirements, high performance HTL materials still remain limited.

Copper(I) thiocyanate (CuSCN) is one material that exhibits a combination of the attractive characteristics mentioned above,[9] and in recent years, has rapidly gained popularity as an HTL.[10] CuSCN is a molecular compound from the metal pseudohalide family, and is a wide bandgap (>3.4 eV) semiconductor with a field-effect hole mobility in the range of 0.01-0.1 $cm^2V^{-1}s^{-1}$.[11,12] This *p*-type material has been successfully utilized in a variety of device types including thin-film transistors (TFTs),[13–15] OLEDs,[16,17] OPVs,[18,19] and metal halide perovskite solar cells.[20–22] Other inorganic *p*-type semiconductors such as hole-transporting metal oxides offer an alternative to metal pseudohalides; examples include copper oxide (Cu_2O), tin monoxide (SnO), and the aforementioned NiO_x.[5,23,24] However, compounds such as Cu_2O and SnO have significantly smaller bandgaps[25–27] relative to CuSCN, which limits their applicability as an HTL due to poor optical transparency. Additionally, metal oxides often require high temperature processing,[28,29] and this property can make them incompatible with temperature sensitive plastic substrates that are utilized in the manufacture of lightweight and flexible electronics.

Alternatives to the above include the organic small molecule, 2,2',7,7'-tetrakis-(N,N-di-*p*-methoxyphenyl-amine)-9,9'-spirobi-fluorene (spiro-MeOTAD); a highly effective[30,31] but extremely expensive hole-transport material. Conventional polymer HTLs such as poly(3,4-ethylenedioxythiophene) polystyrene sulfonate (PEDOT:PSS) offer a more cost-effective option. PEDOT:PSS is comparable to CuSCN in exhibiting good optical transparency, low surface roughness and solution processability. However, with a typical pH in the range of 1.5-

2.5 as specified by commercial suppliers, the acidic nature of this organic HTL can lead to unstable device performance and reduced device lifetime.[32–34] Furthermore, the semi-metallic character of PEDOT:PSS creates an efficiency loss mechanism in OPVs and OLEDs due to its inability to function as an electron blocking layer. In contrast, the large conduction band minimum energy of CuSCN (-1.5 to -1.8 eV) imposes an energy barrier that limits the flow of electrons between the active layer and anode, and therefore minimizing recombination losses.[4-7] Hence, due to the shortcomings of most conventional HTLs, it is essential to identify new hole-transporting materials that enable the fabrication of highly efficient and stable opto/electronics. Since CuSCN possesses a unique combination of physical properties that makes it a much promising HTL, exploring related chemical compounds is a logical first step in the development of a new HTL.

Here we report on a novel HTL material, copper (I) selenocyanate (CuSeCN), which combines all the aforementioned advantageous properties. CuSeCN is a metal pseudohalide that is structurally similar to CuSCN, but the literature on this selenium-based pseudohalide is extremely limited. A handful of reports detail the synthesis,[35] solubility,[36] and chemical structure[37,38] of CuSeCN. To this end, Kilmartin and Wright has examined the formation of CuSeCN on a copper anode,[37] while Manceau and Gallup have investigated a copper-selenium precipitate that forms during the removal of selenocyanate from water.[38] However, charge transport properties and applications of CuSeCN have not been experimentally investigated. In two recent publications, Tsetseris used density-functional theory (DFT) calculations to probe the stability of various CuSeCN crystalline phases, including two-dimensional polymorphs.[39,40] Here, we focus on the most stable three dimensional CuSeCN phases and provide detailed DFT results on their structures and electronic properties. Next, we chemically synthesize this compound, develop a solution-processing route to the fabrication of thin films, and use a variety of material characterization techniques to experimentally verify that CuSeCN

is a chemically stable, *p*-type semiconductor. Finally, we demonstrate the potential of this novel semiconductor for applications in microelectronics and optoelectronic devices by fabricating CuSeCN-based TFTs, OPVs and OLEDs. To the best of our knowledge, this is the first experimental demonstration of CuSeCN as a semiconducting material and the first report of electronic devices based on CuSeCN. The work highlights metal pseudohalides as an unconventional class of chemical compounds that must be investigated further in the search for next-generation HTLs.

2. Density-Functional Theory Calculations

DFT calculations were performed using the code Quantum Espresso (QE),[41] projector-augmented waves[42,43] (PAW) to describe the interactions between valence electrons and ions, and the Perdew-Burke-Ernzerhof (PBE) generalized-gradient approximation (GGA) exchange-correlation functional.[44] The concurrent relaxation of atomic positions, unit cell volume, and shape of the unit cell was performed with an energy cut-off (E_c) of 75 Ry for the plane-wave basis of wavefunctions. Sampling of reciprocal space employed the tetrahedron method[45] for electronic density of states (DOS) calculations and the Monkhorst-Pack scheme[46] of special *k* points for the other studies. Selective tests showed that the results presented below are well-converged with respect to E_c and the number of *k*-points. Similar methodology has been used in recent studies on 3D-CuSCN and 2D-$Mo(SCN)_2$.[47,48]

As noted above, experiments have reported both the α-orthorhombic and β-wurtzite phases in the case of CuSCN.[49] We thus probed the stability and structural details of these two phases also for CuSeCN. It turns out that the wurtzite structure is more stable than the α-phase with the energy difference of 34 meV per chemical formula between the two cases. It should be noted that this difference is smaller than the one (52 meV) obtained between the α- and β-

phases of CuSCN.[47,48] Hence, though the wurtzite structure is expected to be the most prevalent polymorph of CuSeCN, the α-phase may well coexist. Indeed, as it will be discussed in the following sections, different CuSeCN samples studied in this work were found in either the α- or β-phase depending on the preparation conditions. Different stacking orders (namely, the so-called 3R, 4H, and 6H polytypes with ABC, ABAC, and ABCACB stacking orders) are almost degenerate in terms of energy (within 1.5 meV per CuSeCN unit) with the wurtzite crystal (which is the 2H polytype with an AB stacking sequence). So, CuSeCN, just like CuSCN,[47,48,50,51] is prone to polytypism.

Table S1 summarizes the theoretical predictions for the lattice parameters of these two phases for CuSeCN, as well as the *z*-coordinates of atoms in the unit cell of β-CuSeCN. The corresponding X-ray diffraction (XRD) patterns obtained are in very good agreement with the experimental data presented in Section 4.[52] The α- and β- structures are shown in the top panels of **Figure 1**. The figure also presents the associated DOS calculated with the PBE-GGA functional and using 16×16×8 and 4×8×8 *k*-grids for the sampling, respectively, of the reciprocal space of α-CuSeCN and β-CuSeCN. The PBE-based energy bandgaps (E_{gap}) for the β- and α-structures are 1.71 eV and 1.75 eV. The more detailed band structure diagram (**Figure S1**) shows that the bandgap of β-CuSeCN is direct (at least at the PBE level of theory).

Naturally, when post-DFT corrections were included by using the PBE0,[53] B3LYP,[54] and HSE[55] hybrid functionals (and 6×6×2 *k*-grids), the calculated E_{gap} values were found to be larger and equal to 3.30 eV, 3.05 eV and 2.60 eV, respectively. All three values evince that β-CuSeCN is a wide bandgap semiconductor. Comparison with measured optical bandgap values (see Section 4.3) show the PBE0 E_{gap} is the closest to the experimentally extracted value.

DFT calculations of native defects in β-CuSeCN, and in particular, copper vacancies, SeCN vacancies and NCSe sequence faults (wherein N and Se positions are inter-changed with

respect to normal SeCN chains in the crystal), were also performed. The results were obtained with two sets of calculations based on large supercells with 24 or 32 atoms. The *p*-type character of CuSCN is believed[11,56] to be associated with the presence of copper vacancies and DFT results confirm this assumption.[47,48] Pertinent DOS results (**Figure S2**) show a similar effect in the CuSeCN case. In particular, copper vacancies of β-CuSeCN shift the Fermi level inside the valence band (VB) and close to its maximum. This key result is consistent with the enhanced hole transport character of β-CuSeCN experimentally determined in this study and will be discussed next. We should note that this feature remains qualitatively the same when the DOS is calculated with the hybrid HSE functional for a supercell with 8 CuSeCN units. A SeCN vacancy, on the other hand, creates a state (shown with an arrow in **Figure S2**) about 0.25 eV below the conduction band (CB) of the material. The corresponding DOS for the NCSe sequence fault is not shown as it does not present significant differences with respect to the defect-free case close to the valence and conduction bands.

3. Chemical Synthesis and Material Processing

CuSeCN was synthesized according to the method detailed by Söderbäck.[35] In brief, this involved the addition of potassium selenocyanate (KSeCN) to a solution of copper (I) ions, freshly prepared by the reduction of copper(II) sulfate ($CuSO_4$) by sodium thiosulfate (NaS_2O_3). The resulting CuSeCN compound was 'greyish-white' in colour and sparingly soluble in water, in agreement with Söderbäck's work. Just like CuSCN, however, CuSeCN is found to be soluble in diethyl sulfide (DES).[18,57–60] As shown in **Figure S3**, a colourless saturated solution formed when CuSeCN was dissolved overnight in DES at a concentration of 10 mg mL^{-1} on a hotplate heated to 50 ˚C and subsequently filtered. When the CuSeCN/DES solution was spin-cast on a glass substrate and annealed at 140 ˚C in a nitrogen atmosphere, an optically

transparent layer was formed (**Figure S3**). CuSeCN layers spin-cast at 800 rpm and annealed 140 ˚C had a typical thickness in the range 12-16 nm, which could be modulated by changing the deposition conditions. This is an important feature and in Section 5 we will briefly discuss the impact of HTL thickness on device performance.

Due to the relatively low solubility of CuSeCN in DES, at room temperature, it was also possible to sequentially spin-cast and anneal multiple layers of CuSeCN in order to deposit HTLs with controlled thickness. Each layer was spin-cast according to the process outlined in the Experimental Section and annealed at 140 ˚C for 20 min. Due to the low boiling point of the DES solvent (90-92 ˚C), layers were first allowed to cool to room temperature (~20 ˚C) for 5 min prior to deposition of the subsequent layer. Three layers were sequentially deposited as a preliminary test; surface profilometer measurements revealed a consistent increase in the mean layer thickness without any observable change in the surface uniformity. However, the thickness of single layer CuSeCN films was found to be sufficient for application in the various opto/electronic devices to be presented in Section 5.

4. Characterization of CuSeCN Powder and Solid Layers

4.1. Elemental Composition, Chemical Bonding and Density of States by XPS

CuSeCN layers were first characterised using X-ray photoelectron spectroscopy (XPS). For this purpose, the solid layer was spin-cast on an Si++ substrate from a DES solution and annealed at 140 ˚C in nitrogen. The survey spectrum of CuSeCN shows all expected core levels as well as Auger lines of both Cu and Se (see **Figure S4**). Core level spectra collected for a CuSeCN film were analysed to investigate the chemical environments present on the film surfaces (**Figure 2a-d**) as well as the electronic structure (**Figure 2e-f**). The Cu $2p_{3/2}$ core line is at a

binding energy (BE) of 933.1 eV, which can be assigned to the Cu 3*d*^{10} configuration in the final state of Cu^{1+} in CuSeCN. Interestingly a small satellite feature is seen at 938.9 eV marked in the figure with an asterisk. This feature is related to Cu^{2+} and the introduction of holes in the Cu 3*d* band, and has been observed in other systems, notably the p-type oxide $CuAlO_2$.[61] The main peak in the Se 3*d* core level at 55.4 eV corresponds to CuSeCN and an additional small contribution at lower BE is found which could be due to a range of different Se environments, e.g. Se-C or Se-Cu. It is not possible to interpret the C 1*s* core level in detail as there is strong overlap with the Se $L_3M_{2,3}M_{4,5}$ Auger lines. Finally, the N 1*s* core level shows a single CuSeCN environment at 398.7 eV.

The valence band (VB) spectrum of CuSeCN (**Figure 2e**) shows a VB maximum (VB_{max}) position of 0.76 eV relative to the Fermi energy (E_F). In order to analyse the specific orbital contributions to different features of the valence band, the XPS spectrum was compared to theoretical calculations. To take into account experimental considerations, theoretically derived partial densities of states (pDOS) of CuSeCN were corrected using one electron atomic cross sections from Yeh and Lindau[62] to account for differences in intensities. A Gaussian broadening of 300 meV was applied, comparable to the minimum experimental broadening at E_F (**Figure S5**). These corrections enable a direct comparison of experiment and theory as shown in **Figure 2f**. The overall shape and BE position of the features in the experiment is well represented by the theory. The top of the VB is dominated by Cu 3*d* states which in the experiment give rise to an intense, asymmetric feature together with a strong Se 4*p* contribution between 4 and 5 eV. Three further features at 6.7, 8.0 and 9.9 eV in the experiment are mainly dominated by Se states with some contribution from Cu *p* and N *s* states. Binding energies corresponding to the three smaller features in the experimental dataset show good correlation with peaks identified as I, II and III in the pDOS plot. In this case, pDOS calculated using the B3LYP hybrid functional as a post-DFT correction produced the best fit to experimental results.

4.2 X-ray Diffraction Analysis

The X-ray diffraction (XRD) patterns obtained experimentally for the CuSeCN powder (inset in **Figure 3a**) and a thin-film, are depicted by black and brown points in **Figure 3a** and **3b**, respectively. The shaded regions in both plots represent the theoretically predicted XRD patterns. For the orthorhombic α-CuSeCN structure and the wurtzite β-CuSeCN structure, *d*-spacings of crystal planes with Miller indices *hkl* were determined[63] using the lattice parameters derived from DFT calculations in Section 2, which are summarized in **Table S1**. Peak positions (2θ) and relative intensities were calculated in accordance with Bragg's law using the Visualization for Electronic and Structural Analysis (VESTA) crystallographic software program.[52]

The as-synthesized CuSeCN powder (**Figure 3a**) was identified as the orthorhombic α-CuSeCN phase where the agreement between the theoretical and experimental results is remarkable. The CuSeCN solid layer (**Figure 3b**), on the other hand, exhibits three measurable peaks (I, II and III) with meaningful signal-to-noise ratio that enabled us to identify the wurtzite β-CuSeCN phase. The relatively high intensity of peak I in the experimental dataset compared to its predicted intensity and the intensity of other experimentally observed peaks indicated that this film is strongly textured. The angular position of the strongest diffraction peak (I) coincides with the theoretical (101) peak, which is significant because the (101) plane shown in the inset in **Figure 3b** is widely reported as a preferential orientation in hexagonal wurtzite crystal systems.[64–66] Therefore, we propose that CuSeCN crystals preferentially grow in the [101] direction in spin-cast solid layers annealed at 140 ˚C.

4.3. UV-Vis-NIR Absorbance Spectroscopy and UV Photoemission Spectroscopy

Figure 4a shows the ultraviolet-visible-near infrared (UV-Vis-NIR) absorbance spectra of CuSeCN layers spin-cast from a DES solution on quartz and annealed at different temperatures (T) in the range 100 to 180 ˚C in nitrogen. All layers appear highly transparent to visible and NIR radiation, with an average transmittance of 94.6% in the wavelength (λ) range 500 to 1400 nm, but with a prominent UV absorption peak at ≈235 nm. It should be noted that the UV absorption of the film annealed at 100 ˚C differed considerably from the other samples (see **Figure S6**), and this coincides with the temperature dependence of electronic properties observed in Section 4, where we present calculations of the field-effect hole mobility in CuSeCN thin-film transistors.

We applied the Tauc method[67,68] to experimentally determine the optical bandgap (E_{OPT}) of CuSeCN layers using transmittance and reflectance data; **Figure 4b** shows the Tauc plots from which E_{OPT} of a CuSeCN layer annealed at 140 ˚C was extracted. In this graph, $(\alpha h\nu)^n$ is calculated using UV-Vis-NIR spectral data and plotted versus incident photon energy ($h\nu$), where α is the absorption coefficient, h is Planck's constant, ν is radiation frequency, and n is equal to 2 for allowed transitions in a direct bandgap semiconductor and ½ for allowed transitions in an indirect bandgap semiconductor. The Tauc plot for an indirect transition (blue curve) exhibits a narrow linear region that offers a poor fit for a bandgap extraction, and furthermore, gives large residual values in the 2.5-3.0 eV low energy region beyond what could be an indirect bandgap. Therefore, we conclude that there is insufficient evidence for an indirect bandgap and propose that CuSeCN solid layers have a direct bandgap in accordance with our DFT calculations in Section 2. A linear fit applied to the Tauc plot for a direct transition (red curve in **Figure 4b**) generated an E_{OPT} value of 3.53 (±0.02) eV, where the specified uncertainty only quantifies the error associated with the data fitting procedure. Additional sources of error in E_{OPT} include any systematic errors introduced by the instrument, the substrate correction factor, and the approximation of the absorption coefficient. Considering these limits of

precision, and noting that E_{OPT} physically differs from the theoretical E_{gap} defined in Section 2 because the latter does not account for quantum mechanical selection rules or exciton binding energies, we conclude that the bandgap extracted from the experimental data is in good agreement with the bandgap predicted in Section 2 using the PBE0 (E_{gap} = 3.30 eV) hybrid functional as a post-DFT correction. E_{OPT} of CuSeCN layers annealed at five different temperatures in the range 100-180 ˚C were determined using Tauc analysis (see **Figure S7**). Despite the aforementioned variation in ultraviolet absorbance highlighted in **Figure S6**, the direct bandgaps extracted from all five datasets agreed within the error margins of the linear fit (±0.02 eV) and provided no evidence for a dependence on annealing temperature. Importantly, these results reveal that CuSeCN is indeed a wide bandgap semiconductor.

Confirming the existence of a wide bandgap was the first fundamental step in verifying the potential of CuSeCN as a next-generation HTL. However, it is also essential to determine the valence band maximum (VB_{max}) energy of CuSeCN in order to assess its compatibility with the workfunction of common electrode materials and the highest occupied molecular orbital (HOMO) energy of organic active layer materials. Therefore, we measured the VB_{max} of a CuSeCN film using an ambient pressure photoemission spectroscopy (APS) system with a UV radiation source. The solid layer was spin-cast from solution in DES and annealed at 140 ˚C in nitrogen. CuSeCN was deposited on indium-tin-oxide (ITO) coated glass because the instrument set-up necessitated the use of conductive substrates, and therefore, using an anode material commonly used in optoelectronic devices was considered most appropriate. The APS instrument contained an integrated Kelvin probe (KP) measurement system, and thus, the work function of the bare ITO surface was measured as 4.8 eV. For the VB_{max} measurement, the CuSeCN sample surface was irradiated by a UV source (wavelengths in the range 200-280 nm) and the photoelectron yield was recorded as a function of incident photon energy. The photoemission signal from the semiconductor was analysed according to Deal, Snow and

Mead's adaptation[69] of the Fowler method,[70] and the result is plotted in **Figure 4c**. VB_{max} of -5.11 (±0.05) eV was extracted from the linear fit, and encouragingly, this value was in good agreement with VB_{max} measurements from two other identically processed samples: -5.09 eV and -5.14 eV. By combining the results from this section with the DFT results from Section 2.1 and the XPS results from Section 4.1, we were able to construct an electronic energy level diagram for CuSeCN, and this is presented in **Figure 4d.**

4.4. Surface Morphology Analysis by Atomic Force Microscopy

CuSeCN layers were spin-cast on to glass substrates from solution in DES and studied via tapping-mode atomic force microscopy (AFM). **Figure 5a-f** presents the surface topography images and corresponding line scans from CuSeCN films annealed at temperatures of 100 ˚C, 140 ˚C and 180 ˚C in nitrogen. CuSeCN films appeared continuous and nanocrystalline, with ellipsoidal grains and no evidence of microscopic pinholes. The surface morphology of CuSeCN layers – the grain size in particular – exhibited a strong dependence on annealing temperature. The typical length (Δx in **Figure 5**) of the elongated crystallites increased from ~35 nm in the film annealed at 100 ˚C to ~80 nm in the film annealed at 180 ˚C. However, the crystallites exhibited a relatively flat structure (platelet-like) in all three samples and formed a smooth surface with a maximum surface height variation (Δz_{max} in **Figure 5**) of only 4-6 nm.

Figure 5g shows the surface height histograms extracted from topography images of CuSeCN layers deposited on glass; the histogram of a bare glass substrate is shown for comparison. As indicated on the diagram, the samples were annealed at temperatures of 100-180 ˚C. These data were obtained using a larger scan area of 5 μm^2 to generate distributions that were a better representation of large-area surface uniformity; the 1 μm^2 images displayed in **Figure 5** have comparatively lower root mean square roughness (R_{rms}). Median surface

height and R_{rms} calculated from the distributions in **Figure 5g** are plotted as a function of annealing temperature in **Figure 5h**. Both variables increased gradually with increasing temperature: the median height ranged from 12.6 nm in the layer with the smallest crystallites (T = 100 ˚C) to 15.7 nm in the layer with the largest crystallites (T = 180 ˚C), while R_{rms} ranged from 3.3 nm in the smoothest film (T = 100 ˚C) to 5.9 nm in the roughest film (T = 180 ˚C). Importantly, the results in this section reveal that CuSeCN films annealed at ≤140 ˚C exhibit excellent surface uniformity with low R_{rms}. This property is essential for opto/electronic device applications because a smooth HTL surface is more likely to produce a defect-free interface with the adjacent organic layer and limit the formation of shunting pathways,[71] which is an important efficiency optimisation process in OPVs and OLEDs.

4.5. Environmental Stability of CuSeCN Layers

The environmental stability of CuSeCN HTLs was examined using two techniques. First, the absorbance spectrum of a CuSeCN film spin-cast on quartz from solution in DES and annealed at T = 140 ˚C was measured using UV-Vis-NIR spectroscopy. The spectrum of the as-deposited film was recorded immediately after moving the sample from the nitrogen atmosphere of the processing environment to the ambient air atmosphere of the spectrometer instrument. Next, another absorbance spectrum was recorded using an identical measurement procedure after exposing the CuSeCN film to ambient air in the laboratory for a time period (t) of one month. The results are presented in **Figure S8**. **Figure S8a** shows that the spectrum recorded at t = 1 month appears to be identical to the spectrum of the as-deposited film recorded at t = 0 min. Transmittance and reflectance data were also recorded at t = 0 min and t = 1 month, and analysed according to the Tauc method detailed in Section 4.3.[67,68] **Figure S8b** shows that after one month of air exposure, the CuSeCN film exhibited a direct E_{OPT} of 3.53 eV. Remarkably, this

value agrees with the bandgap extracted from the as-deposited sample (**Figure 4b**) within the small error margins (±0.02 eV) associated with the linear fit. If CuSeCN decomposed or converted to another chemical compound in the presence of atmospheric oxygen and humidity, a change in the absorbance spectrum or the optical bandgap would be expected. Promisingly, these results indicated no evidence for the sample having undergone such a chemical reaction, and hence, confirmed the excellent environmental stability of CuSeCN solid layers.

APS and KP measurements were used to further study the effects of ambient air exposure on a CuSeCN solid layer spin-cast on ITO-coated glass from a DES solution and annealed at T = 140 ˚C (**Figure S9**). VB_{max} and E_F of the CuSeCN film was monitored using methods outlined in Section 4.3[69,70] and recorded as a function of air exposure time. The sample chamber of the KP-APS instrument facilitated both ambient air and nitrogen-flushed measurements, and hence, the CuSeCN sample was initially transferred from the nitrogen-filled glovebox (fabrication environment) to the nitrogen-flushed KP-APS chamber inside a metal sample holder with an air-tight seal. The as-deposited film was measured at time (t) = 0 min in a nitrogen-flushed atmosphere, after which the sample was exposed to air and left in the ambient air environment of the laboratory. Measurements made after t = 1 hr, t = 1 day and t = 1 week of air exposure are summarized in **Figure S9a**. Notably, the VB_{max} energy remained at a constant value of -5.1 (±0.05) eV over the 7 days measurement period, indicating no evidence of a change in chemical composition. This important observation further confirmed that CuSeCN is stable in air and does not degrade upon exposure to ambient humid air (≈50% relative humidity). E_F of the as-deposited film was recorded as lying ΔE = 0.6 (±0.1) eV above the VB_{max} using the KP-APS system, but a value of ΔE = 0.76 eV was extracted from the XPS spectrum in **Figure 2f**. The small discrepancy of 0.06 eV is primarily attributed to the different atmospheric conditions inside the two measurement systems: high vacuum (2×10^{-9} mbar) in the XPS sample chamber and an N_2/O_2 environment at atmospheric pressure in the KP-APS sample chamber.

E_F of CuSeCN was observed to deepen gradually towards the VB_{max} upon air exposure, from -4.5 to -4.6 eV during the first hour, and then to -5.1 eV over a time period of one week. In contrast, when temporal variation of the Fermi level in CuSCN was monitored using the same experimental procedure (see **Figure S9b**), E_F was found to deepen rapidly towards the VB_{max} (-5.4 eV) from -4.6 eV to -5.3 eV during a time period of only 10 min – a substantial atmospheric *p*-doping effect over a short time scale. Evidently, CuSeCN exhibits superior environmental stability relative to CuSCN. Surface charge-transfer doping of semiconductor materials via molecular adsorption in ambient air environments is widely reported, with the charge-transfer models proposed considering a variety of redox mechanisms.[72–74] VB_{max} energies of CuSCN and CuSeCN are comparable to the electrochemical potential associated with reactions such as the O_2/H_2O redox couple proposed by Chakrapani *et al.*,[72] which is approximately -5.3 eV in humid environments that are lightly acidic due to the presence of atmospheric CO_2. Since the molecular adsorption properties of the CuSeCN surface and the exact pH of the laboratory environment are unknown, the dominant redox mechanisms underpinning the observed difference in atmospheric *p*-doping efficiency should be explored in future studies**.**

5. Application of CuSeCN in Opto/Electronic Devices

5.1. CuSeCN Thin-Film Transistors

Bottom-gate, bottom-contact (BG-BC) transistors (**Figure 6a**) were fabricated using CuSeCN as the channel semiconductor layer that was spin-cast from a DES solution and annealed in nitrogen. The channel length (*L*) and width (*W*) of the resulting devices were 5 µm and 10 mm, respectively. **Figure 6b** shows a schematic diagram of a staggered top-gate, bottom-contact (TG-BC) architecture with an Al gate electrode and Au S-D electrodes thermally evaporated on a glass substrate. This architecture employed a commercially available, optically transparent

polymer dielectric – poly(methyl methacrylate) [PMMA][75,76] – as the gate insulator. Notably, the TG-BC transistor is a semi-transparent device and utilizes a fabrication process that is compatible with the use of flexible plastic substrates.

Transfer and output curves of a BG-BC CuSeCN transistor are presented in **Figure 6c** and **Figure 6d**, respectively. The transfer characteristics (i.e. I_D versus gate voltage (V_G)) were recorded at two source-drain voltages (V_D) corresponding to the linear (lin) and saturation (sat) operating regimes. In accordance with our environmental stability results from Section 4.5, transistors were fabricated and characterized in a nitrogen-filled glovebox to prevent the exposure of CuSeCN to atmospheric *p*-dopants. Devices containing a CuSeCN semiconductor layer annealed at 140 ˚C exhibited excellent hole-transport characteristics with low turn-on voltage (V_{ON}) of +5 V, small threshold voltage (V_{TH}) of -3 V, clear channel current saturation, high on/off current ratio (10^4), and reasonable operating voltages (~|40| V) for a 200 nm-thick SiO_2 dielectric. The key operating parameters are summarized in **Table S2**. The mean and maximum field-effect hole mobility (μ) calculated in the saturation regime were 0.0016 $cm^2V^{-1}s^{-1}$ and 0.0019 $cm^2V^{-1}s^{-1}$, respectively, and encouragingly, are comparable to mobility values reported in the literature for similarly structured CuSCN TFTs.[13] However, these transistors exhibited noticeable hysteresis – an effect previously reported in BG-BC CuSCN devices due to charge trapping at the interface between the semiconductor and the SiO_2 dielectric.[13] This undesirable characteristic was an additional motivation for subsequently adapting the TG-BC architecture shown in **Figure 6b**.

The transfer and output characteristics of a TG-BC CuSeCN transistor are presented in **Figure 6e** and **Figure 6f**, respectively. All devices characterized had identical channel dimensions of W = 30 µm and L = 1000 µm. The low dielectric constant ($\varepsilon_r \approx 3.3$) of the thick (≈600 nm) insulating PMMA polymer layer necessitated the use of large operating voltages (V_{max} = |100| V). However, this non-ideality could easily be resolved by optimizing the PMMA

layer thickness[77] or replacing PMMA with a high-k dielectric[75] in future studies. Compared to the transfer characteristics of BG-BC devices (**Figure 6c**), the relatively lower maximum I_D measured in the TG-BC configuration (**Figure 6e**) is primarily attributed to the 60× smaller *W:L* ratio of the channel in the latter device type. Importantly, devices containing a CuSeCN layer annealed at 140 ˚C exhibited good hole-transporting characteristics with low voltage turn-on (V_{ON} = -8 V), clear channel current saturation, and considerably lower hysteresis relative to the BG-BC transistors.

The effects of semiconductor annealing temperature (*T*) were also investigated using the TG-BC architecture shown in **Figure 6b**. Transfer characteristics recorded in the saturation regime for TFTs containing CuSeCN layers annealed at temperatures in the range of 100-180 ˚C are shown in **Figure 6g**, and key operating parameters are summarized in **Table S2**. Further significant trends are highlighted in **Figure S10**, where four parameters (μ_{sat}, on/off ratio, V_{ON} and V_{TH}) are plotted as a function of annealing temperature. Transistors containing CuSeCN layers annealed at 100 ˚C performed poorly with small on/off current ratio (8), large V_{ON} of -53 V, large V_{TH} of -68V, and low field-effect hole mobility (μ_{sat} = 2×10^{-5} $cm^2V^{-1}s^{-1}$). In contrast, transistors containing CuSeCN layers annealed at 140 ˚C performed significantly better and *T* = 160 ˚C produced the best device performance. For the latter, on/off current ratios were $\approx10^3$, the typical V_{ON} was -5 V, V_{TH} was -25 V and μ_{sat} approached 0.001 $cm^2V^{-1}s^{-1}$. Evidently, higher annealing temperatures of 140-180 ˚C lead to a remarkable enhancement in the transistor operating parameters. The poor hole-transport properties of CuSeCN films annealed at 100 ˚C coincide with the notable change in ultraviolet absorbance observed at this temperature (see Section 4.3), and is a possible indication of structural differences in CuSeCN layers annealed at $T \leq 100$ ˚C, which should be investigated further in future studies.

An interesting point to consider is the dramatic change in threshold voltage with annealing temperature in TG-BC CuSeCN transistors, as evident from **Figure 6g** and **Figure**

S10. We propose that the observed variation in V_{TH} is likely to arise from a temperature dependence in the formation of deep charge traps and native defects in CuSeCN. Notably, a large positive shift in the threshold voltage (ΔV_{TH} = +43 V) was measured when the annealing temperature of CuSeCN was increased from 100 ˚C to 160 ˚C. It is known that the threshold voltage is partly associated with the V_G required to fill charge traps.[78,79] Hence, the favourable change in V_{TH} is partly attributed to the influence of *T* in deep trap formation, which means that fewer deep hole traps exist in the channel when CuSeCN layers are annealed at 140-160 ˚C. This hypothesis is consistent with previous reports on deep trap formation in inorganic semiconductors such as metal oxides, and its impact on TFT performance.[79–81] Interestingly, **Table S2** shows that the subthreshold swing (*SS*) of TG-BC transistors is substantially improved when CuSeCN layers are annealed at higher temperatures (140-160 ˚C). As there is a negative correlation between the *SS* of a TFT and the trap concentration in the channel, the dramatic decrease in *SS* observed upon raising *T* from 100 ˚C to 140-160 ˚C provides additional evidence of a temperature dependent trap formation process, which yields a reduced deep trap density at higher *T*. Furthermore, as the concentration of vacancies and impurities in an inorganic semiconductor lattice can depend on annealing temperature,[82,83] an increase in the concentration of Cu vacancies formed in CuSeCN at high *T* (140-160 ˚C) could contribute additional free holes to the system. The additional free holes in the TFT channel would also be manifested as a positive shift in V_{TH}. The unfavourable changes in V_{TH}, μ and *SS* observed upon increasing *T* from 160 ˚C to 180 ˚C should be examined in future to assess the thermal stability of CuSeCN at high temperatures (≥180 ˚C), and probe possible changes in the ionic composition, chemical bonding and crystalline phase.

Since the AFM results (**Figure 5**) discussed previously revealed that spin-cast CuSeCN layers have a small grain size (20-90 nm), it is important to consider the impact of grain size on charge transport. A smaller grain size usually reduces the carrier mobility of an inorganic

semiconductor material, and this is attributed to the increased grain boundary density, and associated scattering, and the possible existence of deep traps at grain boundaries.[84–87] Notably, in TFTs containing CuSeCN annealed at 140 ˚C, the maximum μ_{sat} measured in the BG-BC devices employing SiO_2 as the dielectric was 0.0019 $cm^2V^{-1}s^{-1}$, while the maximum μ_{sat} measured in the TG-BC devices employing a PMMA dielectric was 0.0006 $cm^2V^{-1}s^{-1}$. Differences in the gate dielectric material must indeed be considered, but it should be noted that the BG-BC devices had a channel length of only 5 µm, but the TG-BC devices had a channel length of 30 µm. Therefore, the latter is more vulnerable to grain boundary limited hole transport due to its ×6 longer channel length,[88,89] and the increased number of grain boundaries within the TFT channel could be a contributing factor to the reduced field-effect hole mobility.

In contrast, there are also reports of enhanced charge-carrier mobility in semiconductor layers with smaller grain sizes,[90] and some authors believe that these observations are consistent with certain aspects of Seto's grain boundary model.[91] Furthermore, we recently discovered that μ_{sat} in CuSCN TFTs containing semiconductor layers processed using an aqueous solvent is 5× larger than the μ_{sat} achieved with a conventional processing method, despite the significantly smaller grain size (~20 nm).[12] Although further work is in progress to investigate this peculiarity, at present the increased μ_{sat} is partly attributed to a significant improvement in CuSCN surface roughness and structural uniformity, and a *p*-doping effect originating from the adsorption of O_2/H_2O molecules via ambient air exposure and aqueous solvent processing. Importantly, CuSeCN layers annealed at 180 ˚C exhibited the largest grain size (**Figure 5**), but surprisingly, higher μ_{sat} was measured in TFTs containing the smaller-grained CuSeCN layers annealed at 140 ˚C. Therefore, while one would normally expect a larger grain size to improve the field-effect hole mobility due to fewer grain boundaries hindering charge transport, it is evident that competing mechanisms and alternative strategies should also be considered. Based on results from previous studies of CuSCN, alternative

processing solvents and depositing methods should be explored as strategies for optimizing the grain size and hole mobility in CuSeCN.

5.2. Organic Photovoltaic Cells with CuSeCN Hole-Transport Layers

CuSeCN solid layers were incorporated into organic bulk-heterojunction (BHJ) solar cells as the HTL, the performance of which was compared with cells based on standard PEDOT:PSS HTLs. CuSeCN was spin-cast from solution in DES and annealed at 140 ˚C in nitrogen. Standard architecture, single-stack OPV devices (**Figure 7a**) were fabricated using poly(3-hexylthiophene-2,5-diyl) [P3HT] as the donor polymer and [6,6]-phenyl-C_{61}-butyric acid methyl ester ($PC_{60}BM$) as the acceptor small-molecule. A second set of OPV cells employing an identical architecture were also fabricated using poly[N-9'-heptadecanyl-2,7-carbazole-alt-5,5-(4',7'-di-2-thienyl-2',1',3'-benzothiadiazole)] [PCDTBT] as the donor material and [6,6]-phenyl-C_{71}-butyric acid methyl ester ($PC_{70}BM$) as the acceptor material. **Figure 7a** also shows the chemical structures of the two light absorbing polymers (P3HT and PCDTBT), while **Figure 7b** shows the energetics of all constituent materials.

First, the P3HT:$PC_{60}BM$ blend solar cells were electrically characterized. **Figure 7c** displays the current density-voltage (*J-V*) characteristics of two identical OPV devices that differ only by the HTL employed, namely, CuSeCN (25 nm-thick) and PEDOT:PSS. The extracted operating parameters are summarized in **Table S3**. While devices based on PEDOT:PSS demonstrated marginally better power conversion efficiency (PCE = 3.6%) with respect to cells containing CuSeCN HTLs (PCE = 3.3%), we note that deposition parameters for the latter are yet to be optimised, and thus, an improvement in device performance would be expected with optimized HTL thickness. Furthermore, an enhancement in the open circuit voltage (V_{OC}) from 0.55 V (PEDOT:PSS) to 0.57 V was observed in cells containing a CuSeCN

interlayer, which is primarily attributed to the deeper VB_{max} energy of CuSeCN (-5.1 eV) relative to the workfunction of PEDOT:PSS (-5.0 eV).[92,93] Hence, these preliminary results reveal the potential of CuSeCN as a novel HTL material for organic solar cell applications.

Next, solar cells that utilized a higher efficiency[94–96] bulk heterojunction blend (PCDTBT:$PC_{70}BM$) and contained either a CuSeCN or PEDOT:PSS HTL were characterized. Here, the impact of CuSeCN HTL thickness (approx. 5, 15 and 25 nm) was briefly investigated. *J-V* curves from four identical OPV devices that differ only by the HTL employed are presented in **Figure 7d**, and the key operating parameters are summarized in **Table S3**. Evidently, cells with a 25 nm-thick CuSeCN HTL produce a maximum PCE of 5.2% that compares well with the efficiency achieved with PEDOT:PSS (PCE = 5.2%), and confirms that CuSeCN could indeed be a more chemically stable alternative to PEDOT:PSS in optoelectronic applications. We primarily attribute the poor performance of cells containing ultrathin (5 nm) and thin (15 nm) CuSeCN HTLs to incomplete coverage of the rough ITO anode surface, which would lead to efficiency losses via the existence of shunting pathways. Notably, the results in **Figure 7d** also indicate that while a 25 nm-thick layer of CuSeCN is sufficient to match the performance achieved with PEDOT:PSS, the effect of increased (>25 nm) HTL thickness should be investigated in future studies. Spin-casting speeds below 500 rpm produced CuSeCN films of non-uniform thickness, and thus, we propose the multilayer deposition procedure outlined in Section 3 as the preferable strategy for optimization of HTL thickness.

Further inspection of **Table S3** reveals that the 25 nm-thick CuSeCN HTL enhanced the maximum short circuit current (J_{SC}) from 11.7 mA cm^{-2} (PEDOT:PSS) to 11.9 mA cm^{-2} in the PCDTBT:$PC_{70}BM$ blend cells. This is primarily attributed to decreased parasitic absorption by the CuSeCN HTL due to its superior optical transparency (94.6% for λ = 500-1400 nm) compared with PEDOT:PSS.[18,19] A small but critical reduction in the fill factor (*FF*) was also observed when PEDOT:PSS was replaced with a 25 nm-thick CuSeCN HTL, which suggested

that spin-casting parameters should be further optimized to improve the surface uniformity for a better interfacial contact with the organic layer. Importantly, our success in demonstrating good *J-V* characteristics using two different organic BHJ blends demonstrates that CuSeCN is compatible with multiple active layer materials, and furthermore, exhibits solvent orthogonality with a solvent (chlorobenzene) that is widely used in the solution processing of organic active layers. Hence, the results in this section pave the way for further studies on CuSeCN as an HTL for organic opto/electronic applications.

5.3. Organic Light-Emitting Diodes based on CuSeCN Hole-Transport Layers

Finally, the suitability of CuSeCN for application as the HIL/HTL in OLEDs, was investigated. **Figure 8a** and **8b** illustrates, respectively, a schematic diagram of the OLED architecture employed and the energy level diagram of the constituent materials. A basic two layer device structure – consisting of an HIL/HTL, an EML, but no electron-transport layer (ETL) – was selected for evaluating the suitability of CuSeCN as the HTL. The devices employed either PEDOT:PSS or 25 nm-thick CuSeCN as the HIL/HTL, and contained a commercially available light-emitting polymer, 'super yellow' poly-(p-phenylenevinylene) [SY-PPV]. **Figure 8c** shows the electroluminescence (EL) spectra for two SY-PPV-based OLEDs based on PEDOT:PSS and CuSeCN as the HIL/HTLs. The spectra were recorded at a bias voltage of 5 V and while the devices were driven at 978 mA cm^{-2} (PEDOT:PSS) and 600 mA cm^{-2} (CuSeCN). Both devices emit yellow light with the EL peaks centered at ≈548 nm. The minor spectral difference observed at wavelengths exceeding 560 nm is attributed to photonic effects that arise from the different optical environments the emitting chromophores are subjected to.[16] Changing the applied voltage was found to have no effect on the EL spectra, suggesting that the recombination zone is well confined in both devices.

Figure 8d shows the current density (mA cm^{-2}) and luminance (cd m^{-2}) versus applied voltage (*J-V-L*) for OLEDs based on CuSeCN (solid line) and PEDOT:PSS (dashed line) HIL/HTLs. The workfunction of PEDOT:PSS is typically reported as -5.0 eV[92,93] with some reports of shallower energy measurements,[97,98] while the highest occupied molecular orbital (HOMO) of SY-PPV lies at -5.4 eV.[99,100] While the hole injection barrier of ≈0.4 eV for PEDOT:PSS is expected to be small enough to form an Ohmic contact, the deeper VB_{max} of CuSeCN (-5.1 eV) is expected to lead to an even lower energy barrier for holes (≈0.3 eV) and as such to an improved hole injection into the HOMO of SY-PPV. Indeed, CuSeCN-based OLEDs exhibit a reduced turn-on voltage of 2 V as compared to 2.8 V for PEDOT:PSS-based devices. Furthermore, the *J-V-L* characteristics reveal that in comparison to CuSeCN-based OLEDs, devices with PEDOT:PSS produced a $\times 10^3$-10^4 higher current density at low voltages, i.e., below turn-on voltage. We attribute this to the excellent electron-blocking properties of CuSeCN (see energy band diagram in **Figure 8b**) which is completely absent in PEDOT:PSS-based devices. This is because the electron affinity of PEDOS:PSS lies at a significantly deeper energy of -3.3 eV,[33,98] which means that electrons from the lowest unoccupied molecular orbital (LUMO) of SY-PPV[99,100] can move towards the anode via the PEDOT:PSS interlayer, leading to an increase in recombination losses. Consequently, the use of PEDOT:PSS as an interlayer usually demands the addition of an adjacent electron blocking layer.[101] Therefore, the unmatched electron blocking property of CuSeCN HIL/HTLs is an important advantage because it saves both material and fabrication costs by eliminating the requirement for a second interfacial layer between the EML and the anode electrode.

Lastly, **Figure 8e** shows the luminous efficiency of OLEDs with CuSeCN and PEDOT:PSS HIL/HTLs. Evidently, CuSeCN-based devices exhibited superior performance as they exhibit higher luminous efficiency compared to the PEDOT:PSS-based OLEDs. Both types of OLEDs steadily improved in efficiency with increasing luminance until the luminance

exceeded 20,000 cd m^{-2}, but notably, the CuSeCN-based device demonstrated a substantially higher luminous efficiency across the entire operating range without the roll-off reported previously for various types of OLEDs.[16] A summary of the performance characteristics is provided in **Table S4**.

6. Conclusions

We report the synthesis and applications of CuSeCN with particular emphasis on the study of its electronic, microstructural and charge transporting properties. DFT calculations predict that three-dimensional CuSeCN can exist as both the α-phase (orthorhombic) and the more stable β-phase (wurtzite), with the latter being a semiconductor with a wide bandgap of ≥3.1 eV. Interestingly, microstructural analysis revealed that as-synthesized CuSeCN powder is mainly composed of the α-phase while solution-cast layers are dominated by the β-phase. Absorption spectroscopy measurements verified the wide-bandgap nature of the β-CuSeCN, while ambient pressure photoemission spectroscopy indicates a VB_{max} close to -5.1 eV. Field-effect charge transport measurements revealed a unipolar hole-transporting character with a maximum hole mobility value of ≈0.002 $cm^2V^{-1}s^{-1}$. When CuSeCN was employed as the HTL in OPVs, the resulting cells were found to perform similarly to control devices made with PEDOT:PSS with a maximum PCE of 5.2%. Finally, OLEDs based on the light-emitting polymer SY-PPY were shown to exhibit dramatically enhanced performance when the PEDOT:PSS hole-injecting layer was replaced with a CuSeCN HTL/HIL. Improved parameters included reduced diode leakage current, reduced turn-on voltage and significantly higher luminance even at low operating voltages. The findings were attributed to the better energy level alignment between CuSeCN and SY-PPY, and the superior electron blocking properties of CuSeCN. In summary, the present study conclusively demonstrated the potential of CuSeCN

as a novel *p*-type semiconductor for use in a wide range of emerging opto/electronic technologies. Consequently, this relatively unexplored group of compounds – metal pseudohalides – should be investigated further in future opto/electronics research.

7. Experimental Section

Synthesis of CuSeCN: To a solution of $CuSO_4.5H_2O$ (5.0 g, 20 mmol) in water (100 mL) was added $Na_2S_2O_3.5H_2O$ (5.0 g, 20 mmol). The resulting green solution was cooled to 0 ˚C and an aqueous solution of KSeCN (1.94 g) was added in small portions. Initially, a blue-black precipitate formed which turned white upon continuous stirring over 20 min. The solid was filtered and washed with water, ethanol and diethyl ether. After drying, a white-grey powder was isolated (2.1 g, 62%). ^{13}C NMR (100 MHz, diethyl sulfide, 25 ^{o}C, ppm): 116.8; ^{77}Se NMR (76 MHz, diethyl sulfide, 25 ^{o}C, ppm): 319.2.

Thin-Film Deposition: Solutions were prepared by dissolving CuSeCN in diethyl sulfide (Merck, 98%) at a concentration of 10 mg mL^{-1}. After stirring the solutions at 50 °C overnight, the saturated solutions were filtered using a 0.1 µm pore size filter. Substrates were solvent-cleaned prior to deposition of CuSeCN using a sequential ultrasonication procedure: an aqueous solution of Decon 90, deionized water, acetone, and isopropanol. The pre-patterned silicon wafers employed in transistor fabrication required an additional cleaning step of an initial acetone rinse to remove the protective resist layer. Next, the samples were dried using a nitrogen flow and UV-ozone treated. CuSeCN precursor solutions were spin-cast at 800 rpm for 60 s inside a nitrogen-filled glovebox, after which the as-spun films were annealed at temperatures in the range 100-180 ˚C for 20 min on a hotplate inside the glovebox. During the fabrication of optoelectronic devices, CuSeCN HTLs were also spin-cast at two other rotation speeds: 500 rpm and 1500 rpm.

X-ray photoelectron spectroscopy (XPS): The surface of a CuSeCN film spin-cast on a solvent-cleaned heavily doped Si++ substrate was characterised using X-ray photoelectron spectroscopy (XPS). The spectra were recorded on a Thermo Scientific K-Alpha^{+} spectrometer

operating at a base pressure of $2x10^{-9}$ mbar. This system incorporates a monochromated, microfocused Al Kα X-ray source (hν = 1486.6 eV) and a 180° double focusing hemispherical analyser with a 2D detector. The X-ray source was operated a 6 mA emission current and 12 kV anode bias. Data were collected at pass energies of 200 eV for survey, 20 eV for core level, and 15 eV for valence band spectra using an X-ray spot size of 400 µm. Samples were mounted using carbon loaded conductive tape, and in addition, a flood gun was used to minimize sample charging. All spectra were aligned using the C 1*s* contribution of adventitious carbon at 285.0 eV. All data were analysed using the Avantage software package.

X-ray diffraction (XRD): The structure and phase of the CuSeCN powder were assessed using a PANalytical X'Pert system (Cu Kα radiation, wavelength = 1.54 Å) at a voltage of 40 kV and a filament current of 40 mA. For analysis the powders were evenly dispersed on a single crystal Si holder. The diffraction patterns were obtained over the 2θ range of 10-50° in steps of 0.04° and subsequently analyzed using Highscore software. A CuSeCN layer was then spin-cast on a highly doped silicon (Si++) substrate and annealed at 140 °C in nitrogen. XRD experiments were performed on the CuSeCN layer in grazing incidence geometry (angle of incidence = 2°) using a SIEMENS D5000 instrument equipped with a Goebel mirror and a Cu Kα X-ray tube. As with the powder measurement, the tube voltage and filament current were 40 kV and 40 mA, respectively.

***Ultraviolet – visible – near-infrared (UV-Vis-NIR) spectroscopy*:** CuSeCN films were deposited on quartz substrates, and measured using a Shimadzu UV-2600 spectrophotometer equipped with an ISR-2600Plus integrating sphere. Transmittance spectra were recorded in the 200-1400 nm wavelength range, and the absorbance was calculated from the logarithm (base ten) of the spectral data. Additionally, reflectance spectra were recorded over an identical range

of wavelengths in order to calculate the optical bandgap of the semiconductor using Tauc analysis. All data were analysed using Origin software.

Tapping-mode atomic force microscopy (AFM): The surface morphology of CuSeCN films spin-cast on glass was studied using an Agilent 5500AFM system, which employed a cantilever with an approximate resonant frequency of 270 kHz and a force constant of 40 N m^{-1}. Topography data were recorded with PicoView scanning probe microscopy control software using scan areas of 1 μm^2 and 5 μm^2. Gwyddion software was used to analyse the AFM images in order to extract line scans, determine grain size, and calculate surface roughness distributions. Surface height data were processed further using Origin software.

Kelvin Probe (KP) measurements and ambient pressure photoemission spectroscopy (APS): E_F and VB_{max} energy in CuSeCN films were measured using KP contact potential difference measurements and APS, respectively. CuSeCN solid layers were deposited on solvent-cleaned ITO-coated glass substrates and full coverage of the conductive ITO was ensured. The instrument comprised of an APS02 Air Photoemission System and a KP Technology SKP5050 Scanning Kelvin Probe, which contained a sample chamber that facilitated both ambient air and nitrogen-flushed measurements. The contact potential difference of CuSeCN was measured relative to that of a polished silver sample, and the Fermi level of CuSeCN was calculated with respect to the workfunction of the reference metal. VB_{max} was determined by exposing CuSeCN samples to UV radiation (λ = 200-280 nm) and recording the photoemission signal from the semiconductor surface as a function of incident photon energy. The APS02 component was continually flushed with nitrogen prior to and during the operation of the UV source to minimise atmospheric oxygen levels, which were carefully monitored to limit the risk of ozone generation. All data were recorded and analyzed using the KP Technology dedicated system software and processed further using Origin software.

Transistor Fabrication and Characterization: Transistors with a BG-BC architecture were fabricated by spin-casting CuSeCN precursor solutions at 800 rpm on pre-patterned silicon wafer substrates. The silicon substrates consisted of a heavily *n*-doped Si gate (n ~ 3 x 10^{17} cm^{-3}), 200 nm-thick SiO_2 gate dielectric, and pre-patterned 30 nm-thick gold S-D contacts with 10 nm-thick ITO adhesion layer. For the TG-BC architecture, 40 nm-thick gold S-D were thermally evaporated on glass using shadow masks, and subsequently, UV-ozone treated to improve hole-injection into the valence band of CuSeCN.[102] CuSeCN films were spin-cast and thermally annealed according to the aforementioned procedure. Poly(methyl methacrylate) [PMMA] (Merck, Mw ~120,000) was dissolved in butyl acetate (Merck, anhydrous, ≥99%) at 80 mg mL^{-1} by stirring overnight, and spin-cast on CuSCN as the dielectric. PMMA films were annealed at 80 ˚C for 1 hour. The devices were completed by thermally evaporating 40 nm-thick aluminium gate electrodes through shadow masks in a high vacuum environment. Devices were electrically characterized at room temperature in a nitrogen-filled glovebox, using an Agilent B2902A parameter analyser. Saturation regime hole mobility (μ_{sat}) values were calculated using the standard gradual channel approximation transistor model:

$$\mu_{sat} = \frac{L}{W C_{ins}} \left[\frac{\partial^2 I_{D(sat)}}{\partial V_G^2} \right] \quad (1)$$

where, L is the channel length, W is the channel width, and C_{ins} is the geometric capacitance of the gate dielectric.

Organic photovoltaic cell fabrication and characterization: Conventional structure organic solar cells were fabricated using PEDOT:PSS and CuSeCN as the HTLs. Specifically, an as-received aqueous dispersion of PEDOT:PSS (CLEVIOS PH 1000, Heraeus) was spin-cast on ITO-coated glass at 4000 rpm and annealed at 140 °C for 10 min in ambient air as a reference HTL film. CuSeCN HTLs were spin-cast on ITO-coated glass at 500-1500 rpm and annealed

at 140 °C in nitrogen. For the P3HT:$PC_{60}BM$ devices, the BHJ active layer was composed of a 1:1 weight ratio blend of P3HT (Merck) and $PC_{60}BM$ (Solenne BV). The blend was spin-cast at 2000 rpm from a 25 mg ml^{-1} chlorobenzene solution, and annealed at 60 ˚C for 30 min in nitrogen. For the PCDTBT:$PC_{70}BM$ devices, the BHJ active layer was composed of a 1:2 weight ratio blend of PCDTBT (1-Material) and $PC_{70}BM$ (Solenne BV), which was spin-cast at 1250 rpm from an 18 mg ml^{-1} 1,2-dichlorobenzene (Merck, anhydrous, 99%) solution in nitrogen. The samples were then placed under a high vacuum (10^{-7} mbar) inside the evaporator chamber, after which the cells were completed by thermal evaporation of a 70 nm-thick Al electrode through shadow masks. *J-V* characteristics were measured using a Keithley 2400 source-meter. The AM1.5 simulated solar illumination was provided by a Sciencetech Inc. Solar Simulator SF300-A, with an active area of 5 mm^2 defined by a metal stencil mask.

Organic light-emitting diode fabrication and characterization: Bottom-emitting OLEDs were fabricated using PEDOT:PSS and CuSeCN as the HIL/HTLs. An as-received aqueous dispersion of PEDOT:PSS (CLEVIOS PH 1000, Heraeus) was spin-cast on ITO-coated glass at 4000 rpm and annealed at 140 °C for 10 min in ambient air as a reference HTL film. CuSeCN HTLs were spin-cast on ITO-coated glass at 500 rpm and annealed at 140 °C in nitrogen. SY-PPV light-emitting polymer (Merck) was dissolved in toluene by heating the mixture at 60 °C. The polymer solution was spin-cast at 2000 rpm for 60 s and annealed at 100 °C for 15 min. The samples were then placed under high vacuum (10^{-7} mbar) inside the evaporator chamber, after which the devices were completed by thermal evaporation of a 10 nm-thick layer of calcium, followed by a 70 nm-thick layer Al, through shadow masks. The *J-V-L* characteristics were measured using a Keithley 2400 source-meter and Minolta CS-100 luminance meter (Lambertian emission is assumed). OLED emission spectra were measured with a calibrated CCD spectrometer (Ocean Optics 2000). All measurements were performed in a nitrogen-filled

sample holder and the active area for each OLED was 4.5 mm^2, which was defined by the overlap of ITO anodes and Ca/Al cathodes.

Supporting Information
Supporting Information is available from the Wiley Online Library or from the author.

Acknowledgements

N.W. and T.D.A. acknowledge financial support from the European Research Council (ERC) AMPRO grant number 280221, and the Engineering and Physical Sciences Research Council (EPSRC) grant number EP/L504786/1. N.W. and T.D.A are also grateful to Prof. Jenny Nelson for constructive discussions and to Prof. James R. Durrant for supplying the PCDTBT polymer. L.T. acknowledges support for the computational time granted from the Greek Research & Technology Network (GRNET) in the National HPC facility – ARIS – under project pr004034-STEM. D.J.P. acknowledges support from the Royal Society for his University Research Fellowship (No. UF100105 and UF150693). D.J.P. and A.R. acknowledge support from the EPSRC (No. EP/M013839/1 and EP/M028291/1).

Received: ((will be filled in by the editorial staff))
Revised: ((will be filled in by the editorial staff))
Published online: ((will be filled in by the editorial staff))

References

[1] Z. Yin, J. Wei, Q. Zheng, *Adv. Sci.* **2016**, *3*, 1500362.

[2] Z. Yu, L. Sun, *Adv. Energy Mater.* **2015**, *5*, 1500213.

[3] A. S. Subbiah, A. Halder, S. Ghosh, N. Mahuli, G. Hodes, S. K. Sarkar, *J. Phys. Chem. Lett.* **2014**, *5*, 1748.

[4] V. Shrotriya, G. Li, Y. Yao, C. Chu, Y. Yang, *Appl. Phys. Lett.* **2006**, *88*, 73508.

[5] M. D. Irwin, D. B. Buchholz, A. W. Hains, R. P. H. Chang, T. J. Marks, *PNAS* **2008**, *105*, 2783.

[6] X. Zhang, F. You, Q. Zheng, Z. Zhang, P. Cai, X. Xue, J. Xiong, J. Zhang, *Org. Electron.* **2016**, *39*, 43.

[7] Q. Zheng, F. You, J. Xu, J. Xiong, X. Xue, P. Cai, X. Zhang, H. Wang, B. Wei, L. Wang, *Org. Electron.* **2017**, *46*, 7.

[8] S. Liu, R. Liu, Y. Chen, S. Ho, J. H. Kim, F. So, *Chem. Mater.* **2014**, *26*, 4528.

[9] P. Pattanasattayavong, V. Promarak, T. D. Anthopoulos, *Adv. Electron. Mater.* **2017**, *3*, 1600378.

[10] N. Wijeyasinghe, T. D. Anthopoulos, *Semicond. Sci. Technol.* **2015**, *30*, 104002.

[11] J. E. Jaffe, T. C. Kaspar, T. C. Droubay, T. Varga, M. E. Bowden, G. J. Exarhos, *J. Phys. Chem. C* **2010**, *114*, 9111.

[12] N. Wijeyasinghe, A. Regoutz, F. Eisner, T. Du, L. Tsetseris, Y. Lin, H. Faber, P. Pattanasattayavong, J. Li, F. Yan, M. A. McLachlan, D. J. Payne, M. Heeney, T. D. Anthopoulos, *Adv. Funct. Mater.* **2017**, *27*, 1701818.

[13] P. Pattanasattayavong, N. Yaacobi-Gross, K. Zhao, G. O. N. Ndjawa, J. Li, F. Yan, B. C. O'Regan, A. Amassian, T. D. Anthopoulos, *Adv. Mater.* **2013**, *25*, 1504.

[14] L. Petti, P. Pattanasattayavong, Y. Lin, N. Münzenrieder, G. Cantarella, N. Yaacobi-, F. Yan, G. Tröster, T. D. Anthopoulos, *Appl. Phys. Lett.* **2017**, *110*, 113504.

[15] P. Pattanasattayavong, G. O. N. Ndjawa, K. Zhao, K. W. Chou, N. Yaacobi-Gross, B. C. O'Regan, A. Amassian, T. D. Anthopoulos, *Chem. Commun.* **2013**, *49*, 4154.

[16] A. Perumal, H. Faber, N. Yaacobi-Gross, P. Pattanasattayavong, C. Burgess, S. Jha, M. A. McLachlan, P. N. Stavrinou, T. D. Anthopoulos, D. D. C. Bradley, *Adv. Mater.* **2015**, *27*, 93.

[17] L.-J. Xu, J.-Y. Wang, X.-F. Zhu, X.-C. Zeng, Z.-N. Chen, *Adv. Funct. Mater.* **2015**, *25*, 3033.

[18] N. Yaacobi-Gross, N. D. Treat, P. Pattanasattayavong, H. Faber, A. K. Perumal, N. Stingelin, D. D. C. Bradley, P. N. Stavrinou, M. Heeney, T. D. Anthopoulos, *Adv. Energy Mater.* **2015**, *5*, 1401529.

[19] N. D. Treat, N. Yaacobi-Gross, H. Faber, A. K. Perumal, D. D. C. Bradley, N. Stingelin, T. D. Anthopoulos, *Appl. Phys. Lett.* **2015**, *107*, 13301.

[20] P. Qin, S. Tanaka, S. Ito, N. Tetreault, K. Manabe, H. Nishino, M. K. Nazeeruddin, M. Grätzel, *Nat. Commun.* **2014**, *5*, 3834.

[21] K. Zhao, R. Munir, B. Yan, Y. Yang, T. Kim, A. Amassian, *J. Mater. Chem. A* **2015**, *3*, 20554.

[22] S. Ye, W. Sun, Y. Li, W. Yan, H. Peng, Z. Bian, Z. Liu, C. Huang, *Nano Lett.* **2015**, *15*, 3723.

[23] E. Fortunato, V. Figueiredo, P. Barquinha, E. Elamurugu, R. Barros, G. Gonçalves, S.-H. K. Park, C.-S. Hwang, R. Martins, *Appl. Phys. Lett.* **2010**, *96*, 192102.

[24] J. Caraveo-Frescas, P. Nayak, H. Al-Jawhari, D. Granato, U. Schwingenschloegl, H. Alshareef, *ACS Nano* **2013**, *7*, 5160.

[25] S.-Y. Sung, S.-Y. Kim, K.-M. Jo, J.-H. Lee, J.-J. Kim, S.-G. Kim, K.-H. Chai, S. J.

Pearton, D. P. Norton, Y.-W. Heo, *Appl. Phys. Lett.* **2010**, *97*, 222109.

[26] Y. Ogo, H. Hiramatsu, K. Nomura, H. Yanagi, T. Kamiya, M. Hirano, H. Hosono, *Appl. Phys. Lett.* **2008**, *93*, 32113.

[27] P. Pattanasattayavong, S. Thomas, G. Adamopoulos, M. A. McLachlan, T. D. Anthopoulos, *Appl. Phys. Lett.* **2013**, *102*, 163505.

[28] D. Muñoz-Rojas, M. Jordan, C. Yeoh, A. T. Marin, A. Kursumovic, L. A. Dunlop, D. C. Iza, A. Chen, H. Wang, J. L. MacManus Driscoll, *AIP Adv.* **2012**, *2*, 42179.

[29] S. R. Thomas, P. Pattanasattayavong, T. D. Anthopoulos, *Chem. Soc. Rev.* **2013**, *42*, 6910.

[30] M. Liu, M. B. Johnson, H. J. Snaith, *Nature* **2013**, *501*, 395.

[31] V. A. Online, P. Schulz, E. Edri, S. Kirmayer, G. Hodes, D. Cahen, A. Kahn, *Energy Environ. Sci.* **2014**, *7*, 1377.

[32] K. Sun, S. Zhang, P. Li, Y. Xia, X. Zhang, D. Du, F. H. Isikgor, J. Ouyang, *J. Mater. Sci. Mater. Electron.* **2015**, *26*, 4438.

[33] A. Garcia, G. C. Welch, E. L. Ratcliff, D. S. Ginley, G. C. Bazan, D. C. Olson, *Adv. Mater.* **2012**, *24*, 5368.

[34] M. P. de Jong, L. J. van IJzendoorn, M. J. A. de Voigt, *Appl. Phys. Lett.* **2000**, *77*, 2255.

[35] E. Söderbäck, *Acta Chem. Scand.* **1974**, *28*, 116.

[36] A. Golub, V. Skopenko, *Russ. Chem. Rev.* **1965**, *34*, 901.

[37] P. A. Kilmartin, G. A. Wright, *Aust. J. Chem.* **1997**, *50*, 321.

[38] A. Manceau, D. L. Gallup, *Environ. Sci. Technol.* **1997**, *31*, 968.

[39] L. Tsetseris, *Phys. Chem. Chem. Phys.* **2016**, *18*, 7837.

[40] L. Tsetseris, *Phys. Chem. Chem. Phys.* **2016**, *18*, 14662.

[41] P. Giannozzi, S. Baroni, N. Bonini, M. Calandra, R. Car, C. Cavazzoni, D. Ceresoli, G. L. Chiarotti, M. Cococcioni, I. Dabo, A. Dal Corso, S. de Gironcoli, S. Fabris, G. Fratesi, R. Gebauer, U. Gerstmann, C. Gougoussis, A. Kokalj, M. Lazzeri, L. Martin-Samos, N. Marzari, F. Mauri, R. Mazzarello, S. Paolini, A. Pasquarello, L. Paulatto, C. Sbraccia, S. Scandolo, G. Sclauzero, A. P. Seitsonen, A. Smogunov, P. Umari, R. M. Wentzcovitch, *J. Phys. Condens. Matter* **2009**, *21*, 395502.

[42] P. E. Blöchl, *Phys. Rev. B* **1994**, *50*, 17953.

[43] G. Kresse, D. Joubert, *Phys. Rev. B* **1999**, *59*, 1758.

[44] J. P. Perdew, K. Burke, M. Ernzerhof, *Phys. Rev. Lett.* **1996**, *77*, 3865.

[45] O. Jepson, O. K. Anderson, *Solid State Commun.* **1971**, *9*, 1763.

[46] D. J. Chadi, L. Cohen, *Phys. Rev. B* **1973**, *8*, 5747.

[47] L. Tsetseris, *J. Phys. Condens. Matter* **2016**, *28*, 295801.

[48] D. Kaltsas, L. Tsetseris, *J. Phys. Condens. Matter* **2017**, *29*, 85702.

[49] M. Kabešová, M. Dunaj-Jurčo, M. Serator, *Inorganica Chim. Acta* **1976**, *17*, 161.

[50] D. L. Smith, V. I. Saunders, *Acta Crystallogr. B* **1981**, *37*, 1807.

[51] D. L. Smith, V. I. Saunders, *Acta Crystallogr. B* **1982**, *38*, 907.

[52] K. Momma, F. Izumi, *J. Appl. Crystallogr.* **2011**, *44*, 1272.

[53] J. P. Perdew, M. Ernzerhof, K. Burke, *J. Chem. Phys.* **1996**, *105*, 9982.

[54] A. D. Becke, *J. Chem. Phys.* **1993**, *98*, 5648.

[55] J. Heyd, G. E. Scuseria, M. Ernzerhof, *J. Chem. Phys.* **2003**, *118*, 8207.

[56] W. Ji, G.-Q. Yue, F.-S. Ke, S. Wu, H.-B. Zhao, L.-Y. Chen, S.-Y. Wang, Y. Jia, *J. Korean Phys. Soc.* **2012**, *60*, 1253.

[57] T. Ding, N. Wang, C. Wang, X. Wu, W. Liu, Q. Zhang, W. Fan, X. W. Sun, *RSC Adv.* **2017**, *7*, 26322.

[58] L.-J. Xu, X. Zhang, J.-Y. Wang, Z.-N. Chen, *J. Mater. Chem. C* **2016**, *4*, 1787.

[59] W. Zhang, Y. Han, X. Zhu, Z. Fei, Y. Feng, N. D. Treat, H. Faber, N. Stingelin, I. Mcculloch, T. D. Anthopoulos, M. Heeney, *Adv. Funct. Mater.* **2016**, *28*, 3922.

[60] J. Cao, H. Yu, S. Zhou, M. Qin, T. Lau, X. Lu, N. Zhao, C. Wong, *J. Mater. Chem.* **2017**, *5*, 11071.

[61] D. J. Aston, D. J. Payne, A. J. H. Green, R. G. Egdell, D. S. L. Law, J. Guo, P. A. Glans, T. Learmonth, K. E. Smith, *Phys. Rev. B Condens. Matter* **2005**, *72*, 195115.

[62] J. Yeh, I. Lindau, *At. Data Nucl. Data Tables* **1985**, *32*, 1.

[63] L. V. Azaroff, M. J. Buerger, *The powder method in X-ray crystallography*; McGraw-Hill Book Company: New York, 1958.

[64] S. O. Brien, M. G. Nolan, M. Çopuroglu, J. A. Hamilton, I. Povey, L. Pereira, R. Martins, E. Fortunato, M. Pemble, *Thin Solid Films* **2010**, *518*, 4515.

[65] M. Caglar, Y. Caglar, S. Ilican, *Phys. Status Solidi C* **2007**, *4*, 1337.

[66] K. Sardar, F. L. Deepak, A. Govindaraj, M. M. Seikh, C. N. R. Rao, *Small* **2005**, *1*, 91.

[67] J. Tauc, R. Grigorovici, A. Vancu, *Phys. Status Solidi B* **1966**, *15*, 627.

[68] B. D. Viezbicke, S. Patel, B. E. Davis, D. P. Birnie III, *Phys. Status Solidi B* **2015**, *252*,

1700.

[69] B. E. Deal, E. H. Snow, C. A. Mead, *J. Phys. Chem. Solids* **1966**, *27*, 1873.

[70] R. H. Fowler, *Phys. Rev.* **1931**, *38*, 45.

[71] P. Peumans, S. R. Forrest, *Appl. Phys. Lett.* **2001**, *79*, 126.

[72] V. Chakrapani, J. C. Angus, A. B. Anderson, S. D. Wolter, B. R. Stoner, G. U. Sumanasekera, *Science (80-.).* **2007**, *318*, 1424.

[73] G. D. Yuan, Y. B. Zhou, C. S. Guo, W. J. Zhang, Y. B. Tang, Y. Q. Li, Z. H. Chen, Z. B. He, X. J. Zhang, P. F. Wang, I. Bello, R. Q. Zhang, C. S. Lee, S. T. Lee, *ACS Nano* **2010**, *4*, 3045.

[74] H. Xu, Y. Chen, J. Zhang, H. Zhang, *Small* **2012**, *8*, 2833.

[75] S.-H. Lee, Y. Xu, D. Khim, W.-T. Part, D.-Y. Kim, Y.-Y. Noh, *ACS App* **2016**, *8*, 32421.

[76] T.-S. Huang, Y.-K. Su, P.-C. Wang, *Appl. Phys. Lett.* **2007**, *91*, 92116.

[77] Y. I. Ran, L. O. U. ZhiDong, H. U. YuFeng, C. U. I. ShaoBo, T. Feng, H. O. U. YanBing, L. I. U. XiaoJun, *Sci. China Technol. Ser.* **2014**, *57*, 1142.

[78] D. Hong, G. Yerubandi, H. Q. Chiang, M. C. Spiegelberg, J. F. Wager, *Crit. Rev. Solid State Mater. Sci.* **2008**, *33*, 101.

[79] J. Zhang, X. F. Li, J. G. Lu, P. Wu, J. Huang, Q. Wang, B. Lu, Y. Z. Zhang, B. H. Zhao, Z. Z. Ye, *AIP Adv.* **2012**, *2*, 22118.

[80] Y. Kikuchi, K. Nomura, H. Yanagi, T. Kamiya, M. Hirano, H. Hosono, *Thin Solid Films* **2010**, *518*, 3017.

[81] M.-F. Lin, X. Gao, N. Mitoma, T. Kizu, O. Y. Wei, S. Aikawa, T. Nabatame, K. Tsukagoshi, *AIP Adv.* **2015**, *5*, 17116.

[82] S. Hwang, J. H. Lee, C. H. Woo, J. Y. Lee, H. K. Cho, *Thin Solid Films* **2011**, *519*, 5146.

[83] J.-S. Lee, Y.-J. Kim, Y.-U. Lee, Y.-H. Kim, J.-Y. Kwon, M.-K. Han, *Jpn. J. Appl. Phys.* **2012**, *51*, 61101.

[84] J. W. Orton, M. J. Powell, *Reports Prog. Phys.* **1980**, *43*, 1263.

[85] F. M. Hossain, J. Nishii, S. Takagi, A. Ohtomo, T. Fukumura, H. Fujioka, H. Ohno, H. Koinuma, M. Kawasaki, *J. Appl. Phys.* **2003**, *94*, 7768.

[86] S. K. Vasheghani Farahani, T. D. Veal, P. D. C. King, J. Ziga-Pérez, V. Muoz-Sanjosé, C. F. McConville, *J. Appl. Phys.* **2011**, *109*, 73712.

[87] Y. Natsume, H. Sakata, *Thin Solid Films* **2000**, *372*, 30.

[88] G. Adamopoulos, A. Bashir, P. H. Wöbkenberg, D. D. C. Bradley, T. D. Anthopoulos, *Appl. Phys. Lett.* **2009**, *95*, 133507.

[89] G. Adamopoulos, A. Bashir, S. Thomas, W. P. Gillin, S. Georgakopoulos, M. Shkunov, M. A. Baklar, N. Stingelin, R. C. Maher, L. F. Cohen, D. D. C. Bradley, T. D. Anthopoulos, *Adv. Mater.* **2010**, *22*, 4764.

[90] M. U, Y.-J. Han, S.-H. Song, I.-T. Cho, J.-H. Lee, H.-I. Kwon, *J. Semicond. Technol. Sci.* **2014**, *14*, 666.

[91] J. Y. W. Seto, *J. Appl. Phys.* **1975**, *46*, 5247.

[92] M. Nakano, A. Tsukazaki, R. Y. Gunji, K. Ueno, A. Ohtomo, T. Fukumura, M. Kawasaki, *Appl. Phys. Lett.* **2007**, *91*, 142113.

[93] A. van Dijken, A. Perro, E. A. Meulenkamp, K. Brunner, *Org. Electron.* **2003**, *4*, 131.

[94] J. S. Moon, J. Jo, A. J. Heeger, *Adv. Energy Mater.* **2012**, *2*, 304.

[95] D. H. Wang, K. H. Park, J. H. Seo, J. Seifter, J. H. Jeon, J. K. Kim, J. H. Park, O. O. Park, A. J. Heeger, *Adv. Energy Mater.* **2011**, *1*, 766.

[96] S. H. Park, A. Roy, S. Beaupre, S. Cho, N. Coates, J. S. Moon, D. Moses, M. Leclerc, K. Lee, A. J. Heeger, *Nat. Photonics* **2009**, *3*, 297.

[97] E. L. Ratcliff, J. Meyer, K. X. Steirer, N. R. Armstrong, D. Olson, A. Kahn, *Org. Electron.* **2012**, *13*, 744.

[98] E. L. Ratcliff, R. C. Bakus II, G. C. Welch, T. S. van der Poll, A. Garcia, S. R. Cowan, B. A. Macleod, D. S. Ginley, G. C. Bazan, D. C. Olson, *J. Mater. Chem. C* **2013**, 6223.

[99] S. Höfle, A. Schienle, M. Bruns, U. Lemmer, A. Colsmann, *Adv. Mater.* **2014**, *26*, 2750.

[100] M. Zhang, S. Höfle, J. Czolk, A. Mertens, A. Colsmann, *Nanoscale* **2015**, *7*, 20009.

[101] R. Jin, P. A. Levermore, J. Huang, X. Wang, D. D. C. Bradley, C. deMello, John, *Phys. Chem. Chem. Phys.* **2009**, *11*, 3455.

[102] S. Rentenberger, A. Vollmer, E. Zojer, R. Schennach, N. Koch, *J. Appl. Phys.* **2006**, *100*, 53701.

Figures

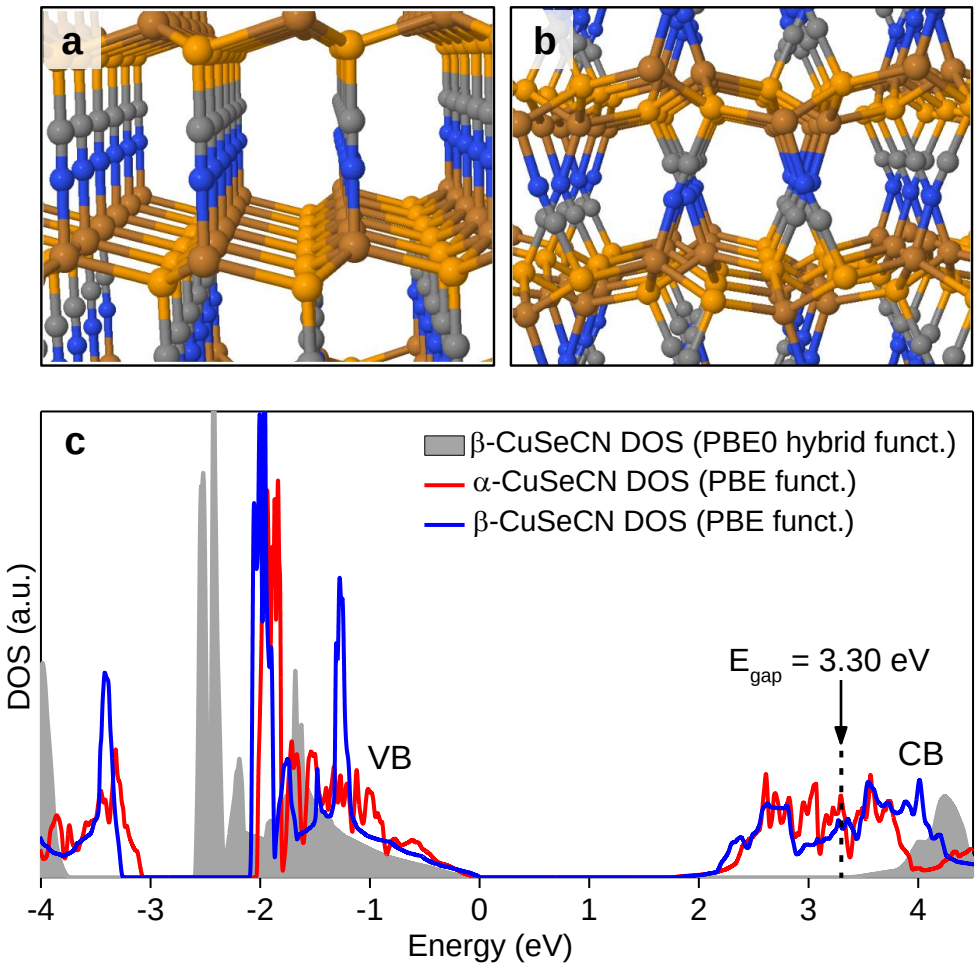

Figure 1. (a) Structure of β-CuSeCN (Cu: brown, Se: yellow, C: grey, N: blue spheres). (b) Structure of α-CuSeCN. (c) Electronic density of states (DOS) for β-CuSeCN (blue line) and α-CuSeCN (red line). Lines are calculated with the PBE functional; shaded area is calculated with the PBE0 hybrid functional. DOS are given in arbitrary units and the zero of energy is set at the valence band (VB) maximum. The conduction band (CB) is also shown.

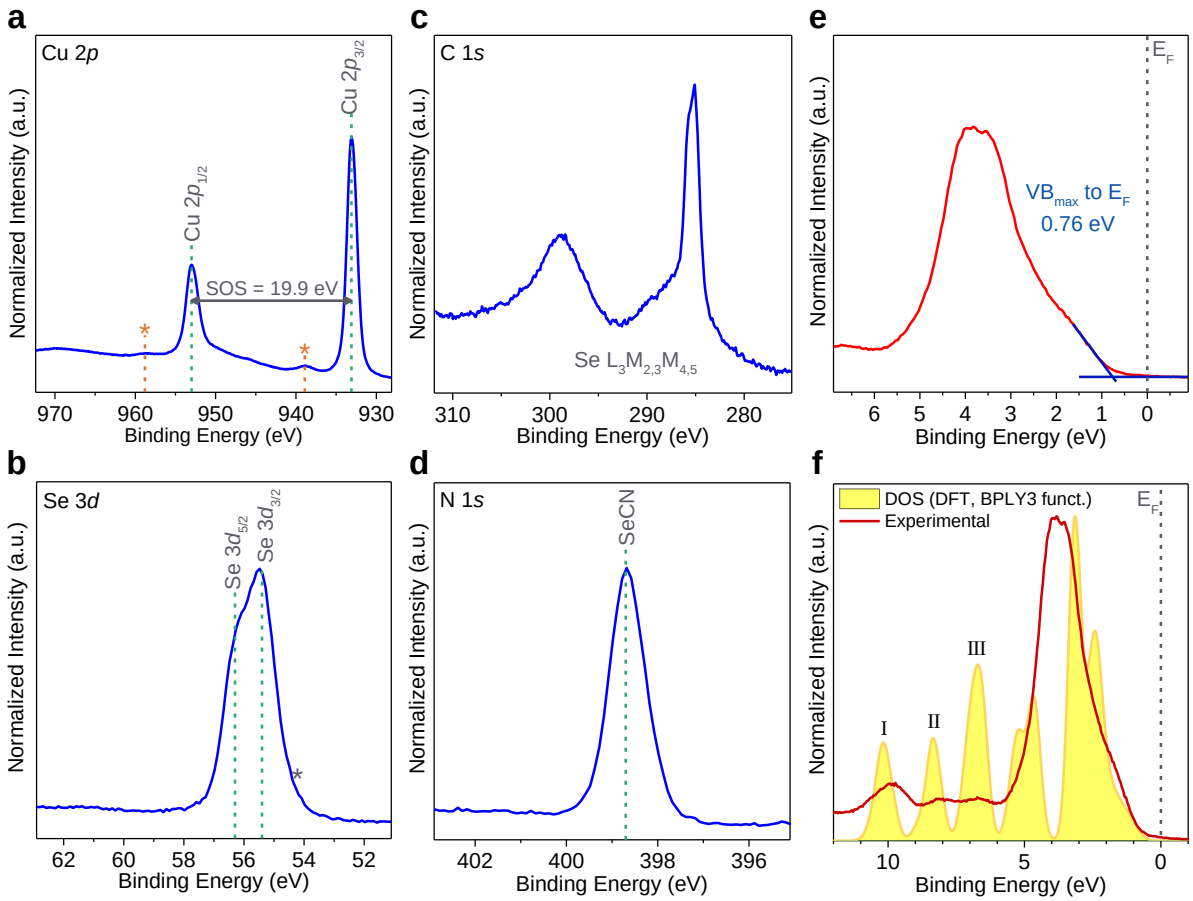

Figure 2. Core level spectra and valence band spectra obtained using XPS of a CuSeCN solid layer spin-cast on Si++ and annealed at 140 °C. (a)-(d) Core level spectra including (a) Cu 2*p*, (b) Se 3*d*, (c) C 1*s*, and (d) N 1*s*. (e) Valence band spectrum showing a comparison of the position of the VB_{max} to the E_F. (f) Valence band spectrum of experimental and one electron cross section corrected density of states (DOS) for CuSeCN from DFT calculations; DOS calculated using the B3LYP hybrid functional as a post-DFT correction generated the best fit.

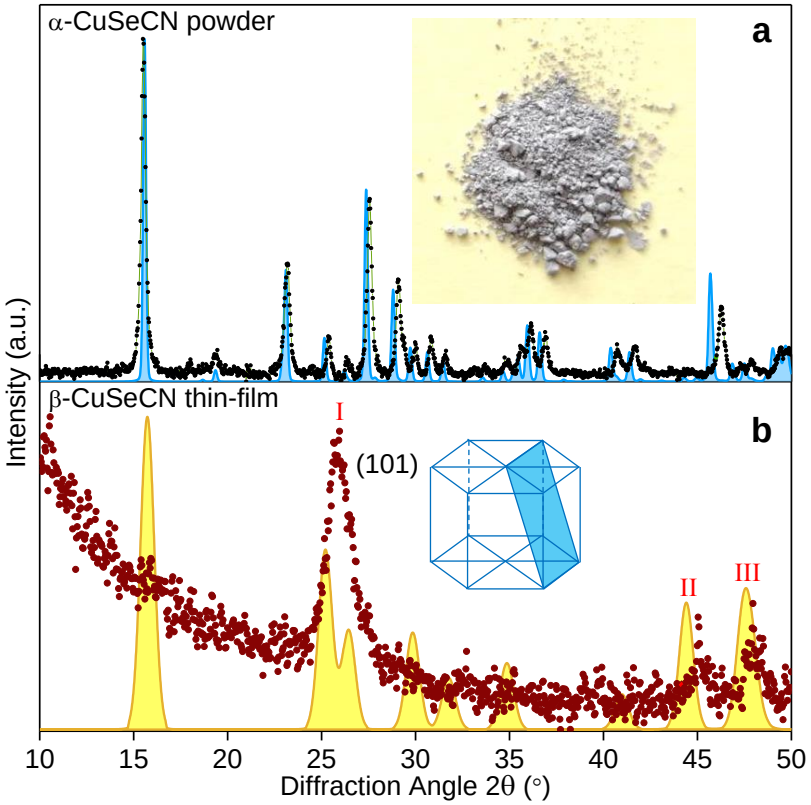

Figure 3. XRD patterns of CuSeCN calculated (shaded area) using DFT results on structural details (i.e., lattice parameters and atomic coordinates) and obtained experimentally (scatter plots) using Cu Kα radiation. (a) XRD pattern from the as-synthesized CuSeCN powder corresponds to the orthorhombic α-phase. Inset: photograph of the as-synthesized, white-grey coloured CuSeCN powder. (b) XRD pattern from a CuSeCN thin-film spin-cast on an Si (100) substrate and annealed at 140 °C; the pattern corresponds to the wurtzite (hexagonal) β-phase. The highest intensity peak in the experimental dataset coincides with the predicted position of the (101) peak that is widely reported as a preferential orientation in hexagonal wurtzite crystal systems.[64–66] Inset: crystal structure diagram indicating the (101) plane.

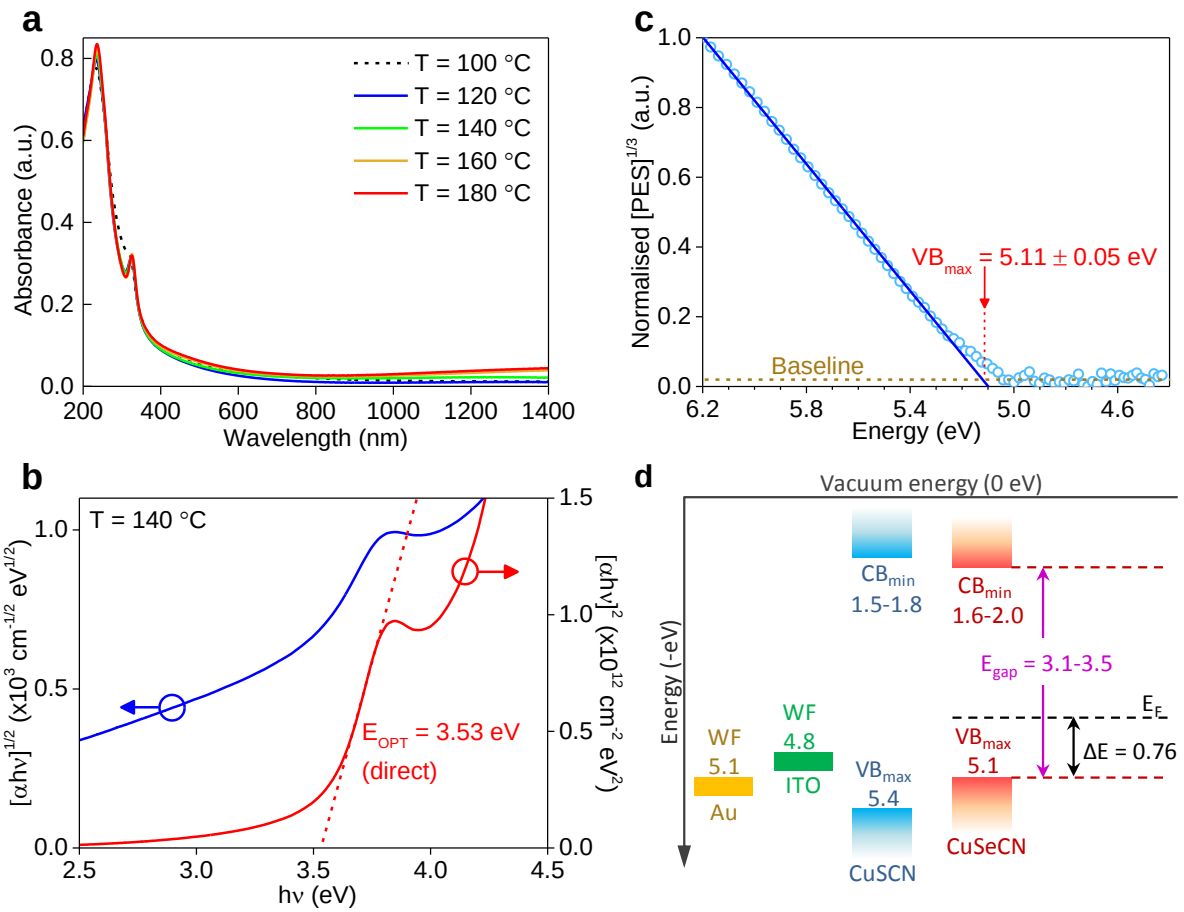

Figure 4. Spectroscopic measurement of the energy level structure in CuSeCN. (a) UV-Vis-NIR absorbance spectra of CuSeCN films spin-cast on quartz and annealed at T = 100-180 °C. (b) Optical bandgap extraction using Tauc analysis of UV-Vis-NIR spectral data from a CuSeCN layer annealed at 140 °C. (c) Ambient pressure UV photoemission spectroscopy of a CuSeCN film spin-cast on ITO and annealed at 140 °C. VB_{max} energy of 5.11 eV is extracted from a linear fit to the cube root of the photoemission signal. (d) Electronic energy level diagram of CuSeCN constructed using our theoretical calculations and experimental data including VB_{max} from (c). E_{gap} is in the range 3.1-3.5 eV according to an experimental value of 3.53 eV from (b) and two values from DFT calculations – 3.05 eV (B3LYP functional) and 3.30 eV (PBE0 functional). E_F was determined as lying 0.76 eV above VB_{max} using XPS. VB_{max} of CuSCN and workfunction (WF) of two electrode materials able to inject holes into CuSeCN are shown for comparison. Conduction band minima (CB_{min}) of the two semiconductors are also indicated.

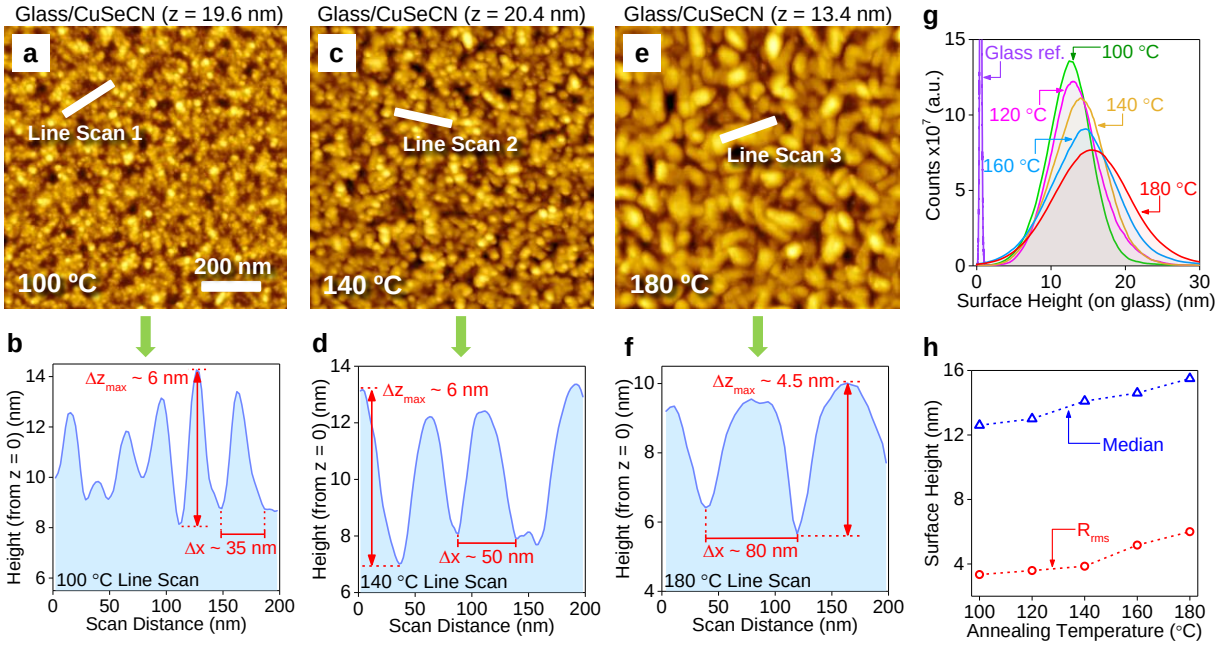

Figure 5. AFM surface topography images (scan area = 1 μm^2), line scans (scan distance = 200 nm), and surface height distributions (scan area = 5 μm^2) of CuSeCN films spin-cast on glass and annealed at T = 100-180 °C. Lighter colours in the topography images correspond to higher regions of the surface and the specified z-values denote the maximum height relative to the minimum at z = 0. (a–b) T = 100 °C. (c–d) T = 140 °C. (e–f) T = 180 °C. (g) Surface height histograms extracted from 5 μm^2 scans; the larger scan area was used to obtain more representative film uniformity data. (h) Median surface height and RMS surface roughness (R_{rms}) calculated from the distributions in (g).

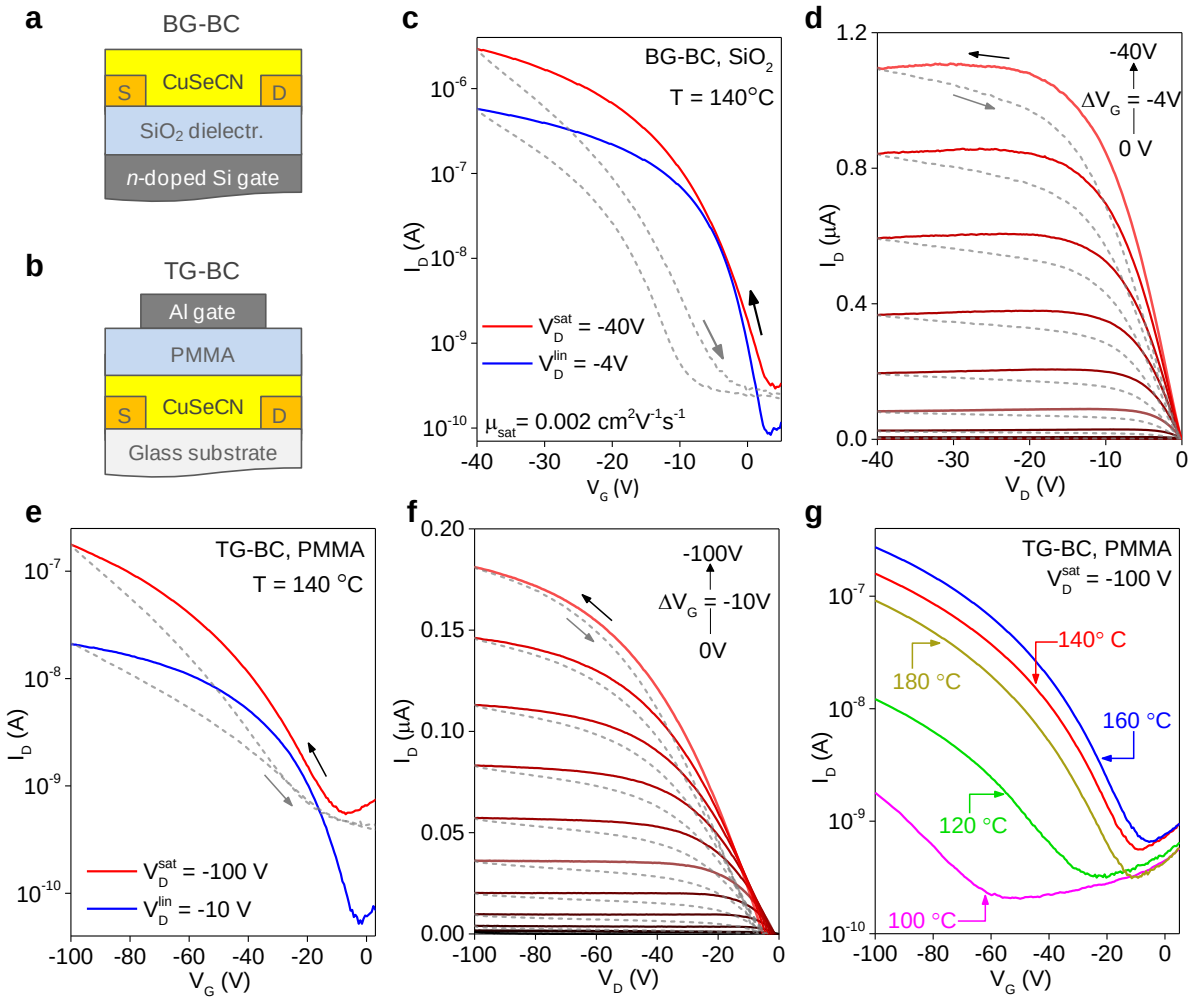

Figure 6. Electrical characterization of thin-film transistors containing spin-cast CuSeCN semiconductor layers annealed at T = 100-180 °C. (a) Schematic of the planar BG-BC architecture. (b) Schematic of the staggered TG-BC architecture. (c) Transfer, and (d) output characteristics of a BG-BC CuSeCN (T = 140 °C) transistor employing the architecture in (a); channel dimensions were W = 10 mm and L = 5 µm. The solid lines indicate forward voltage sweeps while the dashed lines indicate reverse voltage sweeps. (e) Transfer, and (f) output characteristics of a TG-BC CuSeCN (T = 140 °C) transistor employing the architecture in (b); channel dimensions were W = 1000 µm and L = 30 µm. (g) Forward sweep (+5 V to -100 V) transfer curves of TFTs employing the TG-BC architecture in (b) and showing how device performance depends on the annealing temperature of CuSeCN. Key parameters are summarised in **Table S2** and **Figure S10**.

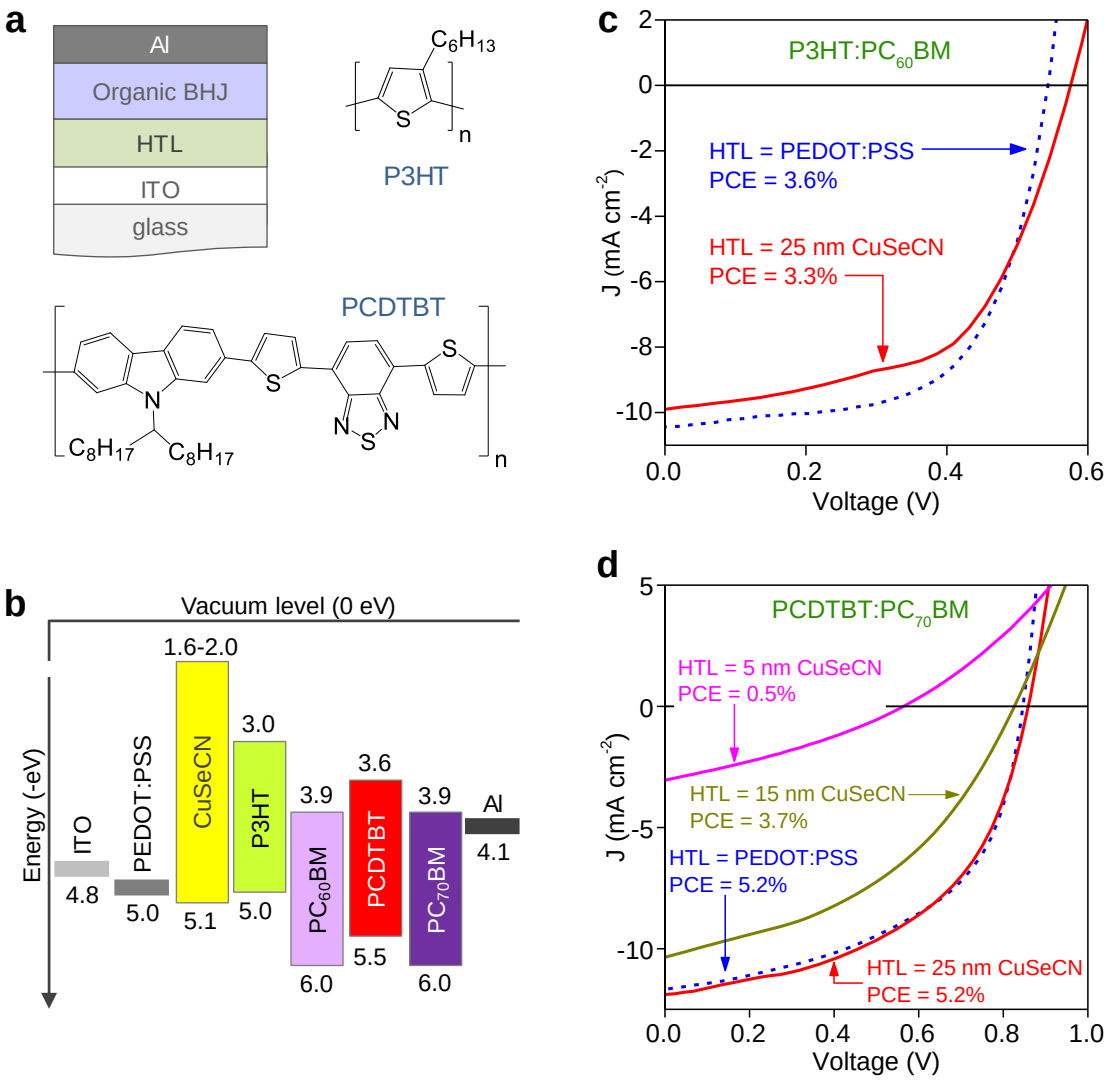

Figure 7. Comparison of OPV performance with CuSeCN and PEDOT:PSS HTLs. (a) Schematic of the standard cell architecture employed. Chemical structures of two active blend components are also shown: (top) P3HT – polymer used in a blend with $PC_{60}BM$, and (bottom) PCDTBT – polymer used in a blend with $PC_{70}BM$. (b) Energetics of the materials employed. (c) *J–V* characteristics measured under AM1.5 simulated solar illumination for standard P3HT:$PC_{60}BM$ solar cells based on two different HTLs, namely, CuSeCN and PEDOT:PSS. (d) *J–V* characteristics measured under AM1.5 simulated solar illumination for standard PCDTBT:$PC_{70}BM$ solar cells based on two different HTLs, namely, CuSeCN and PEDOT:PSS. The effect of CuSeCN HTL thickness was briefly investigated: the plot shows a comparison of *J-V* curves obtained with 5 nm, 15 nm and 25 nm-thick CuSeCN HTLs.

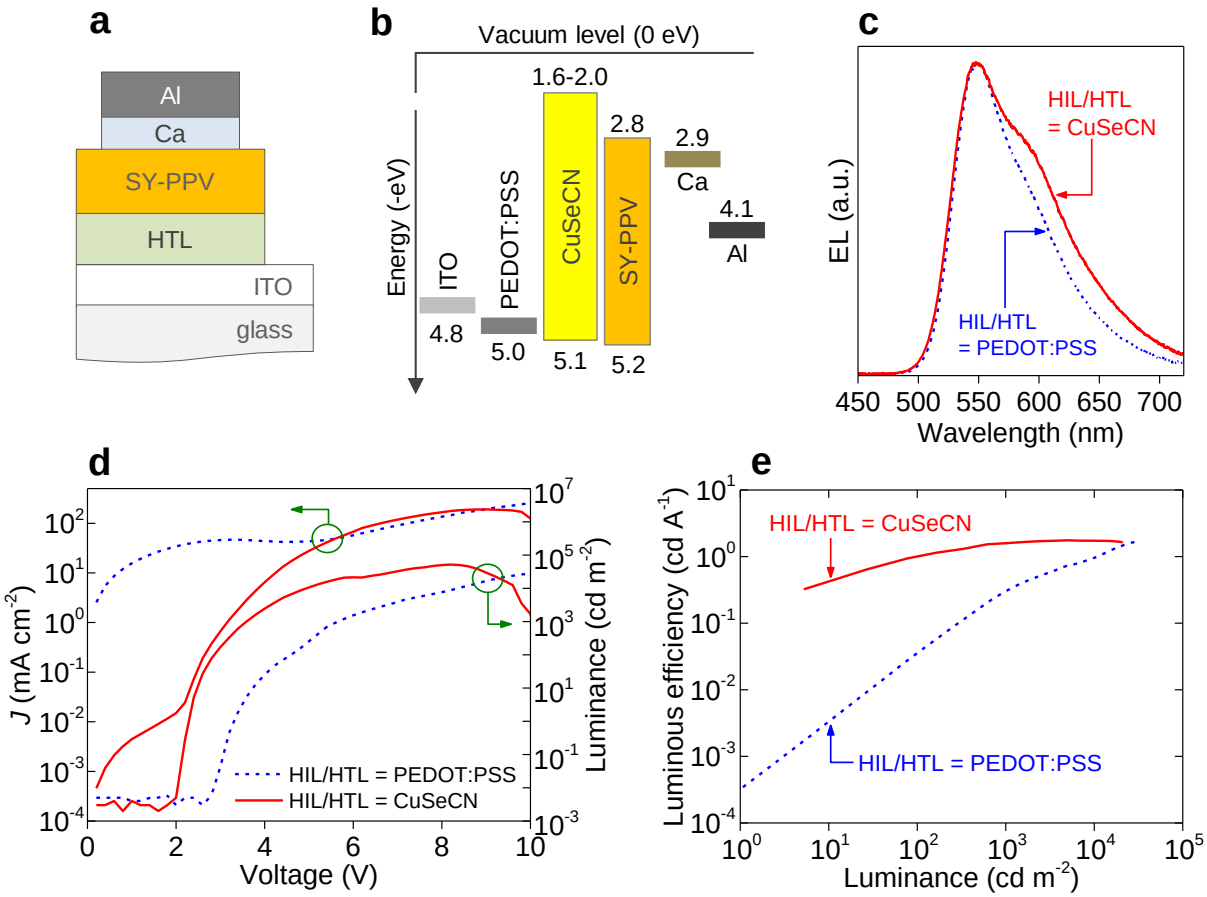

Figure 8. Comparison of OLED performance with CuSeCN and PEDOT:PSS HIL/HTLs. (a) Schematic of the bottom-emitting architecture employed. The light-emitting polymer in the emissive layer is 'super yellow' poly-(p-phenylenevinylene) [SY-PPV]. (b) Energetics of the materials employed. (c) EL spectra for SY-PPV emission from the structure in (a) with either PEDOT:PSS or CuSeCN as the HIL/HTL. EL of SY-PPV with PEDOT:PSS and CuSeCN were recorded 978 mA cm^{-2} and 600 mA cm^{-2}, respectively. (d) Comparison of *J-V-L* characteristics for OLEDs with PEDOT:PSS and CuSCN HIL/HTLs. (e) Luminous efficiency (units: cd A^{-1}) versus luminance (units: cd m^{-2}) characteristics for OLEDs with PEDOT:PSS and CuSCN HIL/HTLs.

Copper (I) selenocyanate was successfully synthesised, studied and applied as a wide bandgap hole-transporting material in transistors, organic solar cells and light-emitting diodes, for the first time. Resulting devices exhibit excellent operating characteristics highlighting the tremendous potential of metal pseudohalides as a new class of highly transparent *p*-type semiconductors.

Keywords: Copper (I) selenocyanate; hole transport layers; organic solar cells; organic light-emitting diodes; transparent semiconductors

*Nilushi Wijeyasinghe, Leonidas Tsetseris, Anna Regoutz, Wai-Yu Sit, Zhuping Fei, Tian Du, Xuhua Wang, Martyn A. McLachlan, George Vourlias, Panos A. Patsalas, David J. Payne, Martin Heeney, and Thomas D. Anthopoulos**

Copper (I) Selenocyanate (CuSeCN) as a Novel Hole-Transport Layer for Transistors, Organic Solar Cells and Light-Emitting Diodes

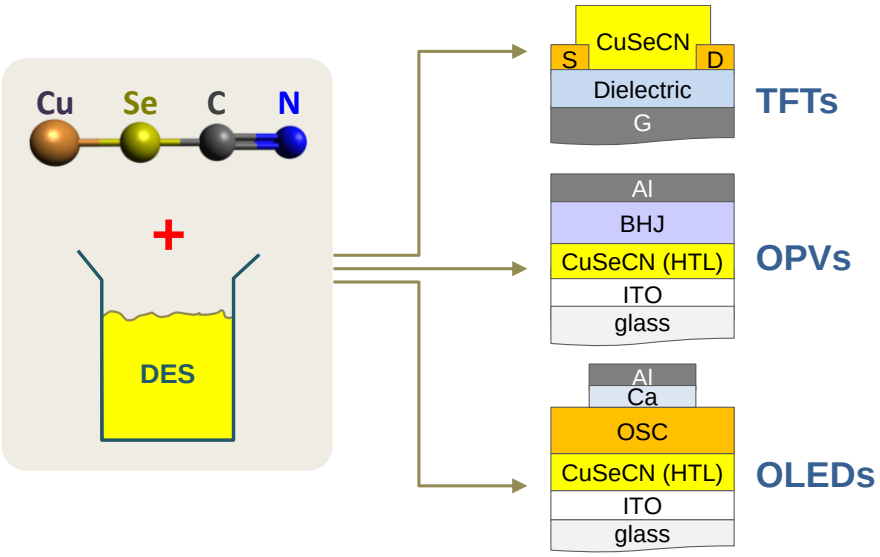

DOI: 10.1002/add manuscript number
Article type: Full Paper

Supporting Information

Copper (I) Selenocyanate (CuSeCN) as a Novel Hole-Transport Layer for Transistors, Organic Solar Cells and Light-Emitting Diodes

*Nilushi Wijeyasinghe, Leonidas Tsetseris, Anna Regoutz, Wai-Yu Sit, Zhuping Fei, Tian Du, Xuhua Wang, Martyn A. McLachlan, George Vourlias, Panos A. Patsalas, David J. Payne, Martin Heeney, and Thomas D. Anthopoulos**

S1. Density Functional Theory Calculations

Table S1. Theoretical predictions of this work for the lattice parameters and *z*-coordinates of atoms (as a fraction of the *c*-axis) for CuSeCN.

Phase	*a* = (Å)	*b* (Å)	*c* (Å)	$u_{Se}(c)$	$u_{C}(c)$	$u_{N}(c)$	*c/a*
β-CuSeCN	4.121	4.121	11.285	0.437	0.274	0.170	2.738
α-CuSeCN[a)]	11.372	7.753	7.081	-	-	-	0.623

a) The *z*-coordinates of atoms for the α-phase of CuSeCN are not included here as there are 8 atoms of each type in the unit cell.

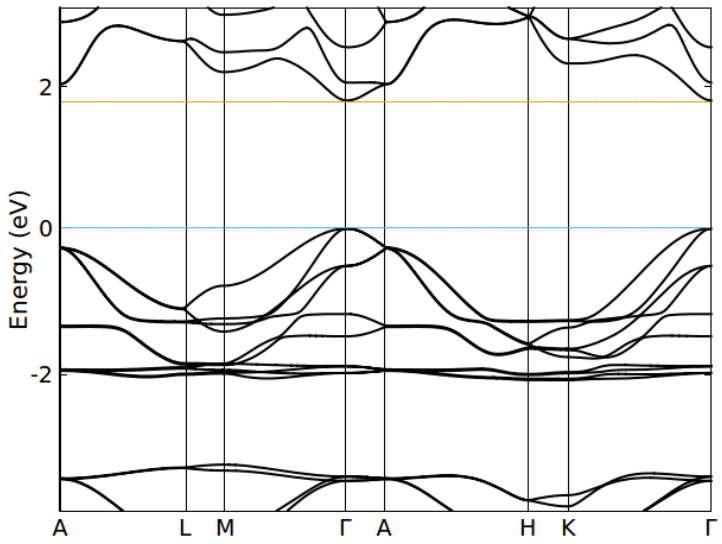

Figure S1. Electronic band structure for β-CuSeCN based on DFT-PBE calculations. Zero of energy is set at the valence band maximum.

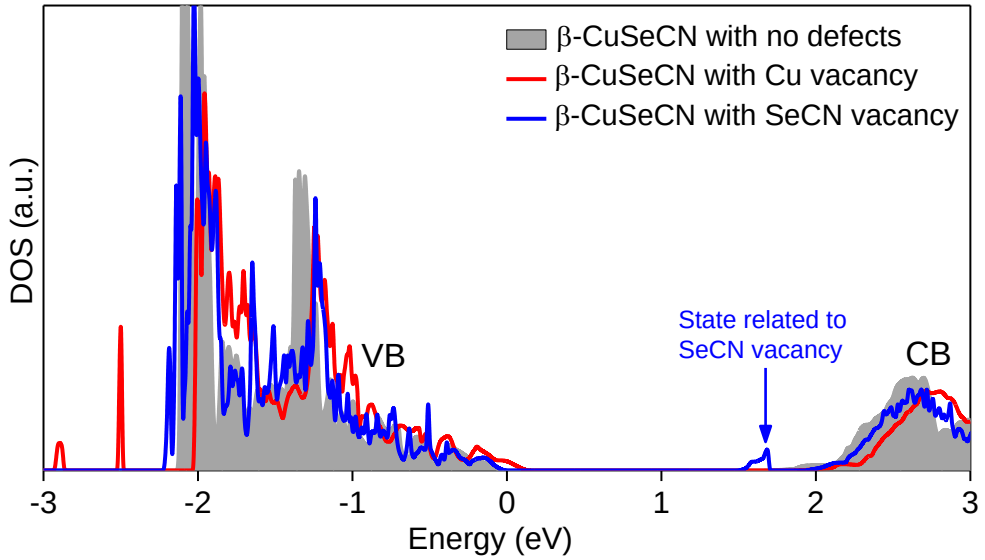

Figure S2. Electronic densities of states (based on DFT-PBE calculations) of β-CuSeCN with no defects (shaded area) and of β-CuSeCN with a Cu vacancy (red line) or an SeCN vacancy (blue line). Zero of energy is set at the Fermi level.

S2. Solution Processing of CuSeCN

Figure S3. Photograph of a 15 nm-thick optically transparent CuSeCN film spin-cast from a diethyl sulfide (DES) solution on a glass substrate and annealed at 140 °C in a nitrogen atmosphere. The image depicts the glass/CuSeCN substrate resting in front of the DES-based CuSeCN solution containing vial.

S3. X-ray Photoelectron Spectroscopy

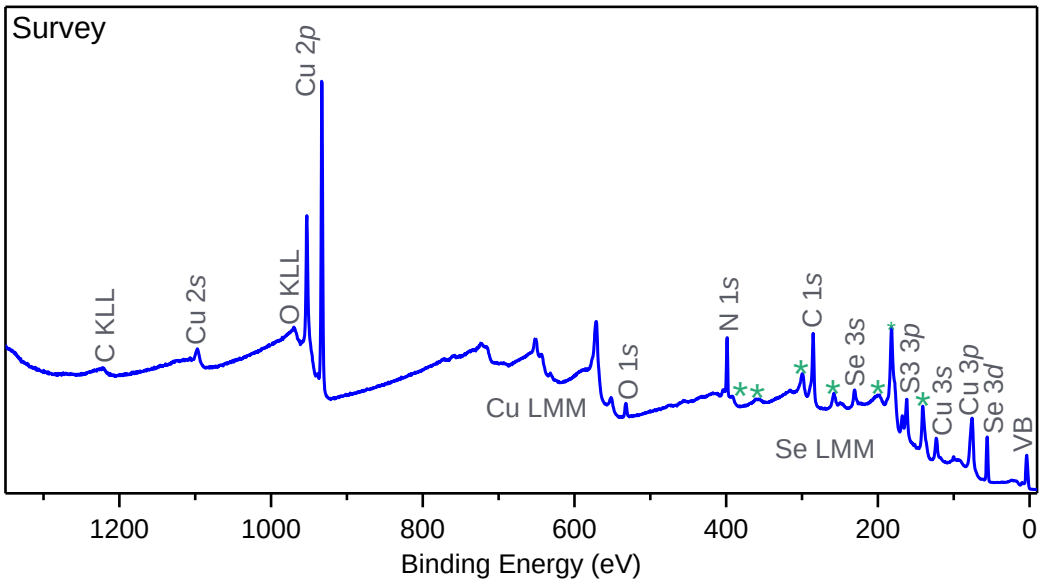

Figure S4. Survey spectra of CuSeCN indicating core levels and Auger lines. The lines marked with an asterisk are major Se Auger lines. The CuSeCN solid layer was spin-cast from a DES solution on an Si++ subtrate and annealed at 140 °C in nitrogen.

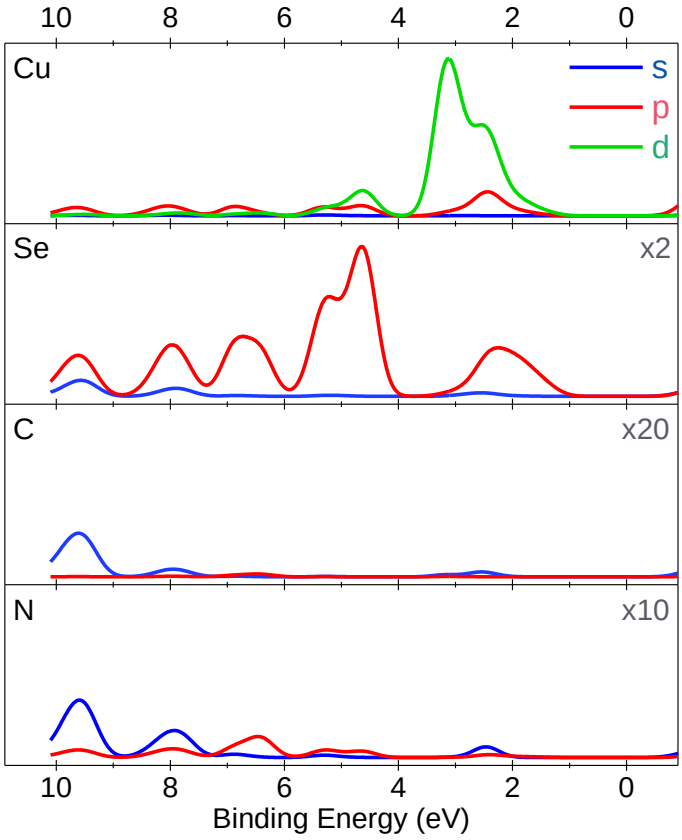

Figure S5. One electron cross section weighted partial densities of states (PDOS) for CuSeCN from DFT calculations.

S4. UV-Vis-NIR Absorbance Spectroscopy

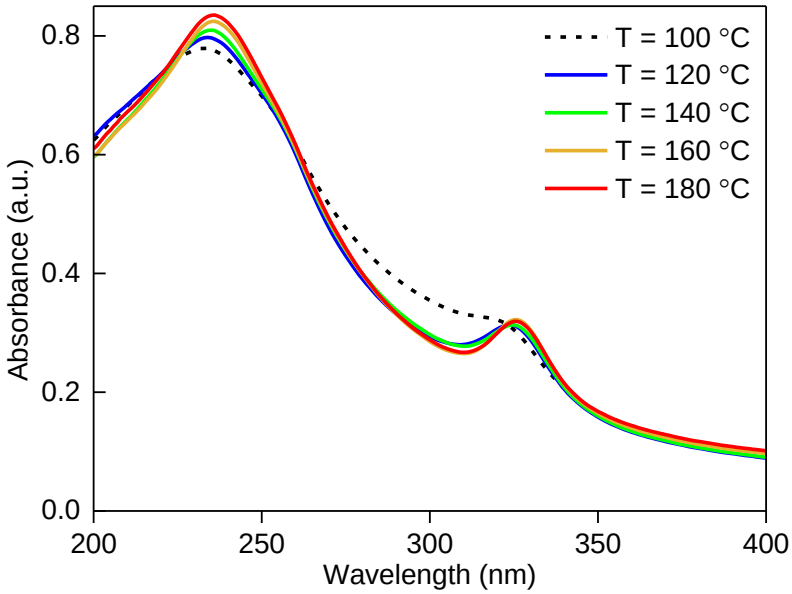

Figure S6. UV-Vis-NIR absorbance of ultraviolet wavelengths by CuSeCN solid layers spin-cast on quartz from DES solutions and annealed at temperatures (*T*) of 100-180 °C in nitrogen.

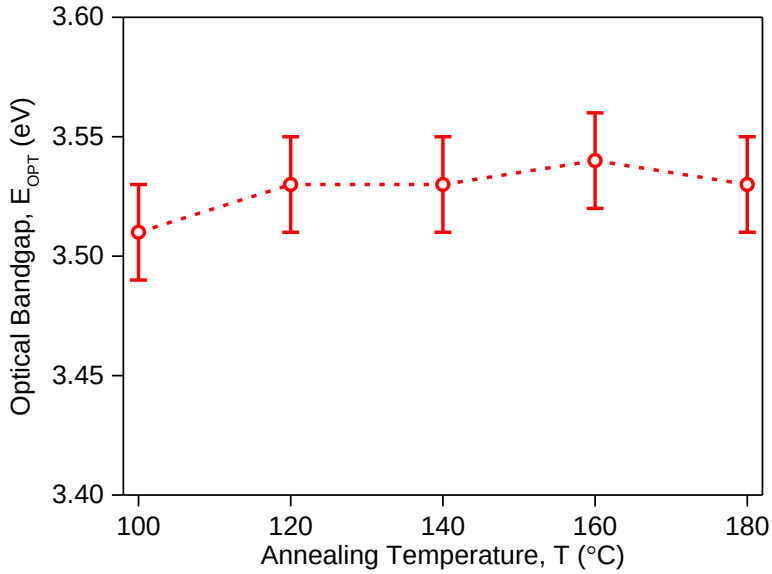

Figure S7. Dependence of the direct optical bandgap in CuSeCN solid layers on annealing temperature. CuSeCN films were spin-cast on quartz from DES solutions and annealed at temperatures of 100-180 °C in nitrogen. Direct optical bandgaps were calculated from UV-Vis-NIR spectral data using Tauc analysis. Error bars quantify the uncertainty (±0.02 eV) associated with the fitting procedure used to determine bandgap values; there is no evidence of temperature dependence in the 100-180 °C range within the limits of uncertainty.

S5. Environmental Stability

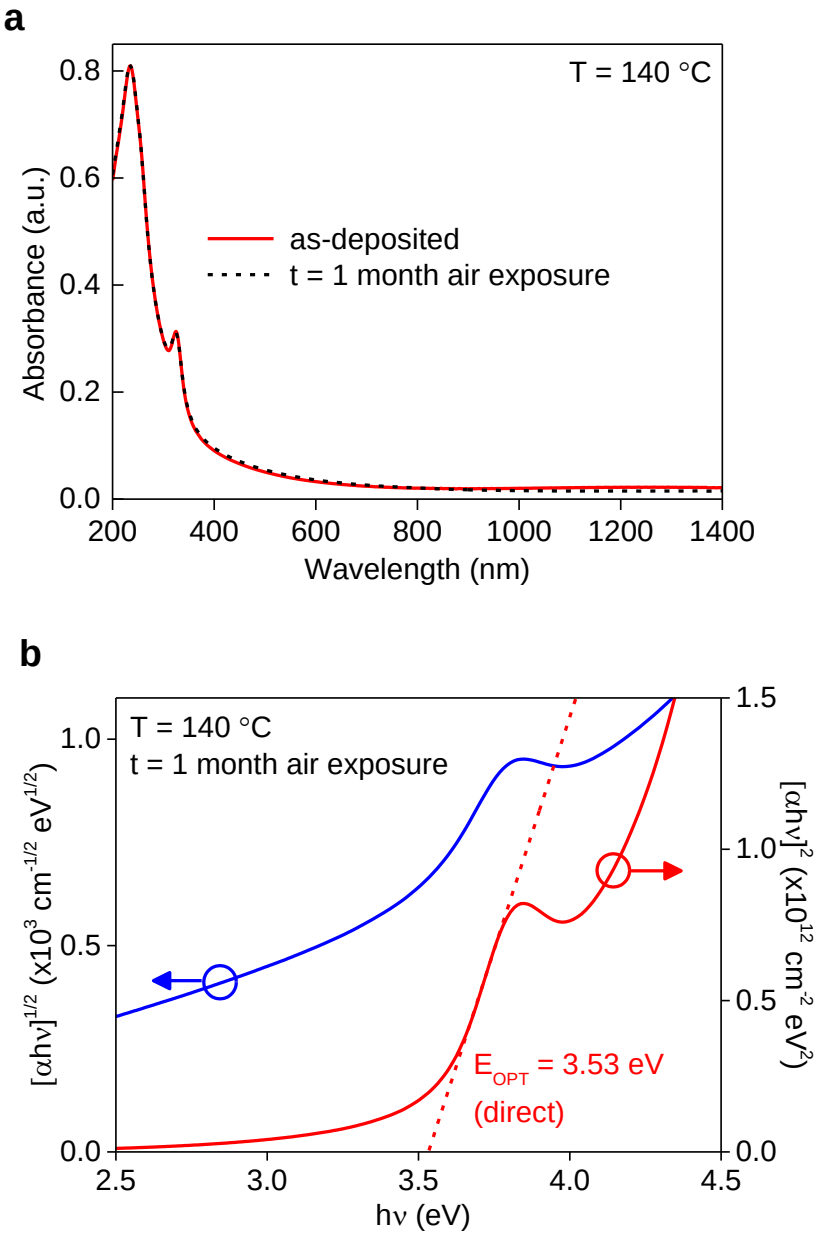

Figure S8. Optical properties of a CuSeCN film, spin-cast on quartz from a DES solution and annealed at 140 °C in nitrogen, were assessed after one month of air exposure. (a) Absorbance spectrum of an as-deposited film at time (*t*) = 0 min, compared with the spectrum of the same film after *t* = 1 month of air exposure in the ambient laboratory environment; the latter exhibited identical absorption features to the former. (b) Optical bandgap extractions from Tauc analysis of spectral data revealed that the direct bandgap value is identical to the value extracted from *t* = 0 min spectra within the range of uncertainty associated with the linear fit (±0.02 eV). As reported in **Figure 4**, the optical bandgap value extracted from the *t* = 0 min spectrum was 3.53 eV. Chemical changes that could occur during the air exposure time are expected to manifest themselves as changes in the absorbance of the material or its optical bandgap. The absence of such evidence indicated that CuSeCN exhibits excellent environmental stability for extended periods of time in the presence of oxygen and humidity. A Tauc plot for an indirect bandgap is also shown for reference and appears identical to the Tauc plot in **Figure 4b**.

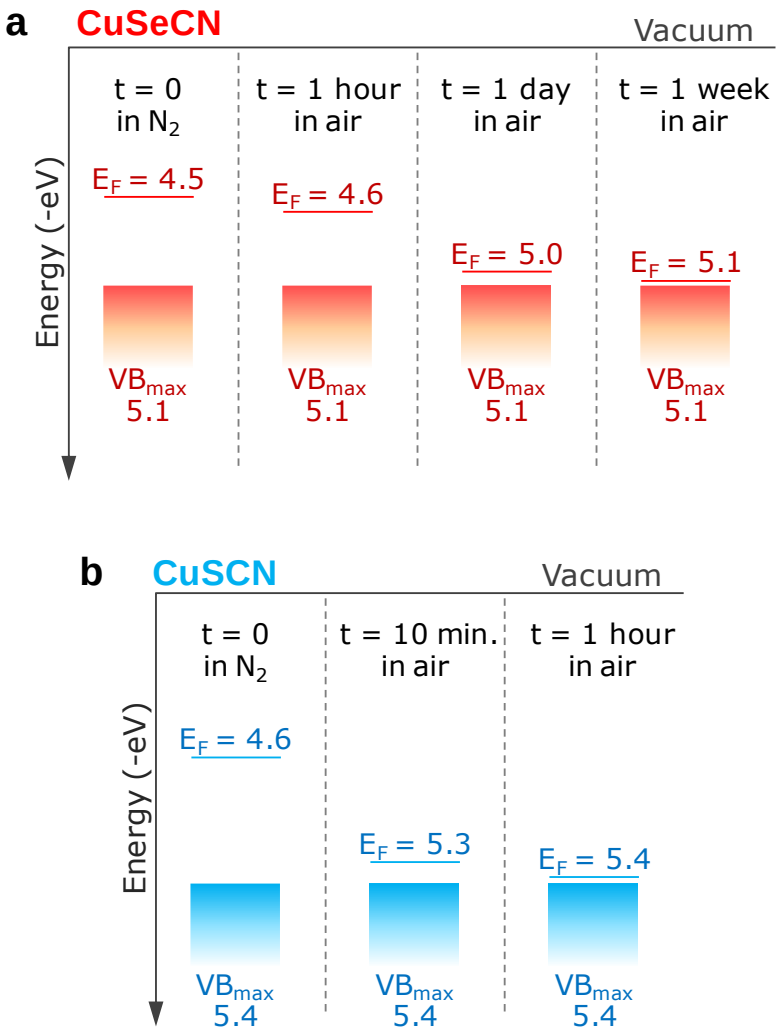

Figure S9. (a) Electronic properties of a CuSeCN film, spin-cast on ITO-coated glass from a DES solution and annealed at 140 °C in nitrogen, were monitored during one week of air exposure. The Fermi level (E_F) and the valence band maximum (VB_{max}) were determined using Kelvin probe (KP) measurements and ambient pressure UV photoemission spectroscopy (APS), respectively. The sample chamber of the KP-APS instrument facilitated both ambient air and N_2-flushed measurements. Therefore, the sample was initially transferred from the N_2-filled glovebox (fabrication environment) to the N_2-flushed KP-APS chamber inside a metal sample holder with an air-tight seal. Measurements of the as-deposited film at time (t) = 0 min were made in an N_2-flushed atmosphere, after which the sample was exposed to air and left in the ambient air environment of the laboratory. Measurements made at t = 1 hr, t = 1 day and t = 1 week were recorded in an air environment. VB_{max} was extracted from a linear fit to the cube root of the photoemission signal and remained at 5.1 eV (±0.05 eV) over the 1 week period. This result further confirmed that CuSeCN exhibited good environmental stability and did not degrade when exposed to O_2 and H_2O. E_F (±0.1 eV) of CuSeCN was observed to deepen towards the VB_{max} over time upon air exposure; this is indicative of an atmospheric *p*-doping process. (b) KP-APS study of a CuSCN film spin-cast on ITO-coated glass from a DES solution and annealed at 100 °C in nitrogen. A significant shift in the Fermi level (-0.7 eV) towards the VB_{max} was observed within 10 min of air exposure. These results indicated that CuSeCN exhibited superior stability in ambient air relative to CuSCN.

S6. Thin-Film Transistors

Table S2. Summary of device parameters extracted from the transfer characteristics of CuSeCN transistors. The channel length and width of planar BG-BC transistors with SiO_2 dielectric were 5 µm and 10 mm, respectively. The channel length and width of staggered TG-BC transistors with PMMA dielectric were 30 µm and 1000 µm, respectively.

Structure	Dielectric	Temp.[a] (°C)	μ_{lin}[b] ($cm^2V^{-1}s^{-1}$)	μ_{sat}[b] ($cm^2V^{-1}s^{-1}$)	On/off ratio[c]	V_{ON}[c] (V)	V_{TH}[c] (V)	SS[d] (V dec^{-1})
BG-BC	SiO_2	140	0.0009 (0.0010)	0.0016 (0.0019)	1×10^4	+5	-3	2
TG-BC	PMMA	100[e]	-	2×10^{-5} (3×10^{-5})	8	-53	-68	17
TG-BC	PMMA	120	2×10^{-5} (3×10^{-5})	9×10^{-5} (0.0001)	50	-23	-36	10
TG-BC	PMMA	140	0.0002 (0.0002)	0.0005 (0.0006)	5×10^2	-8	-26	8
TG-BC	PMMA	160	0.0002 (0.0003)	0.0006 (0.0008)	7×10^2	-5	-25	7
TG-BC	PMMA	180	9×10^{-5} (0.0001)	0.0003 (0.0004)	4×10^2	-12	-33	11

[a] Annealing temperature of CuSeCN.
[b] Mean values obtained from three TFTs; data from the 'champion' device is given in brackets.
[c] Mean values obtained from three TFTs; saturation regime data.
[d] Mean values obtained from three TFTs; linear regime data.
[e] Channel current and signal-to-noise ratio too low to extract meaningful values for μ_{lin} or *SS* from the linear regime data. *SS* was estimated at 17 V dec^{-1} from saturation regime data.

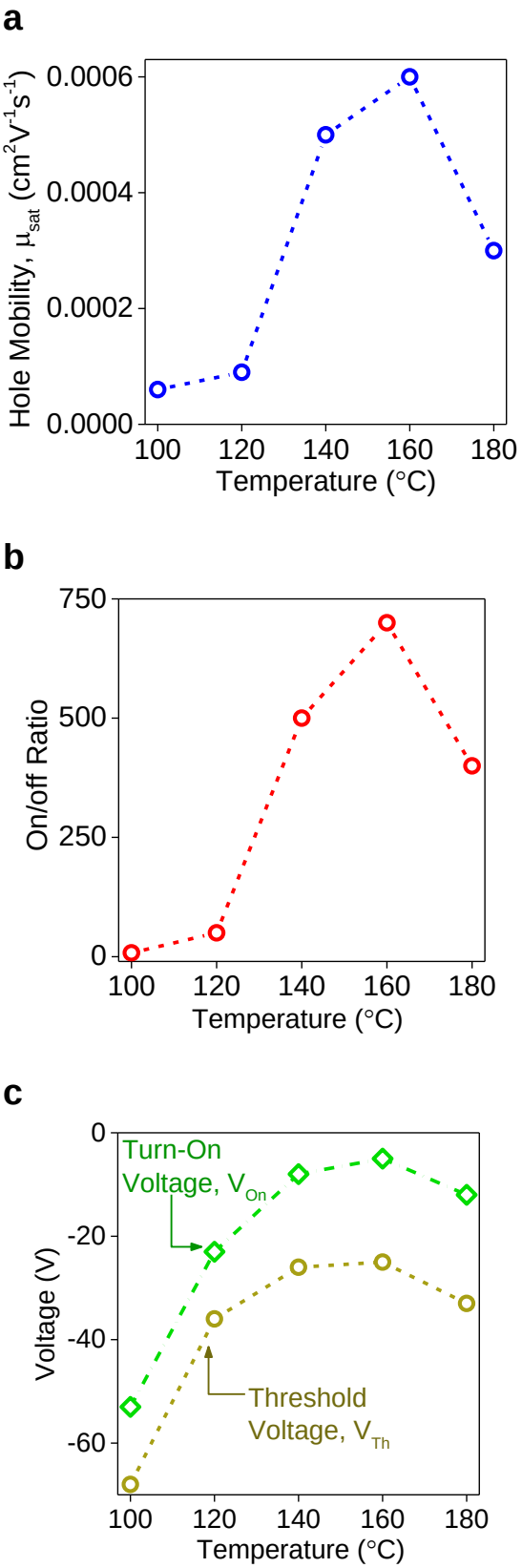

Figure S10. Temperature dependence of four key transistor parameters from staggered TG-BC transistors with a CuSeCN semiconductor and PMMA dielectric. Mean values extracted from the saturation regime datasets and summarised in **Table S2** are plotted here to illustrate the trends. The channel length and width of devices were 30 µm and 1000 µm, respectively. (a)

Field-effect hole mobility, μ_{sat}. (b) On/off channel current ratio. (c) Turn-on voltage, V_{ON}, and threshold voltage, V_{TH}.

S7. Organic Photovoltaic Cells

Table S3. Summary of operating parameters for P3HT:$PC_{60}BM$ blend and PCDTBT:$PC_{70}BM$ blend OPV cells made with different HTLs, measured under AM1.5 simulated solar illumination.

Organic BHJ	HTL[a)]	J_{SC} (mA cm^{-2})	V_{OC} (V)	*FF*	PCE (%)
P3HT:$PC_{60}BM$	PEDOT:PSS	10.1 (10.5)	0.55 (0.55)	62.0 (63.5)	3.5 (3.6)
P3HT:$PC_{60}BM$	CuSeCN, 25 nm	9.9 (10.0)	0.57 (0.57)	56.3 (59.0)	3.2 (3.3)
PCDTBT:$PC_{70}BM$	PEDOT:PSS	11.6 (11.7)	0.86 (0.86)	52.0 (52.5)	5.2 (5.2)
PCDTBT:$PC_{70}BM$	CuSeCN, 25 nm	11.6 (11.9)	0.85 (0.86)	50.0 (51.0)	4.9 (5.2)
PCDTBT:$PC_{70}BM$	CuSeCN, 15 nm	9.3 (10.4)	0.82 (0.84)	42.0 (43.0)	3.3 (3.7)
PCDTBT:$PC_{70}BM$	CuSeCN, 5 nm	2.6 (3.0)	0.49 (0.57)	31.0 (32.4)	0.4 (0.5)

[a)]Mean values obtained from two to four cells of each type that exhibited correct solar cell function; data from the 'champion' cell is given in brackets.

S8. Organic Light-Emitting Diodes

Table S4. Summary of operating parameters for 'super yellow' SY-PPV OLEDs containing PEDOT:PSS and 25 nm-thick CuSeCN HIL/HTLs.

HIL/HTL	Turn-On [V]	Voltage [V] @ 1 cd m^{-2}	Leakage Current [mA cm^{-2}] @ 1 V	Luminance [cd m^{-2}] @ 8 V	Luminous Efficiency [cd A^{-1}] @ 1000 cd m^{-2}
PEDOT:PSS	2.8	3.3	16	7,900[a)]	0.3[b)]
CuSeCN	2.0	2.3	0.004	53,000	1.6

[a)] Maximum luminance of 29,000 cd m^{-2} achieved at 10 V.

[b)] Maximum luminous efficiency of 1.7 cd A^{-1} achieved at 29,000 cd m^{-2}. (OLEDs with CuSeCN HIL/HTL achieved 1.7 cd A^{-1} at 1,500 cd m^{-2}).